Understanding the Links among the Magnetic Fields, Filament, Bipolar Bubble, and Star Formation in RCW 57A Using NIR Polarimetry

Chakali Eswaraiah[1,2,3] , Shih-Ping Lai[1] , Wen-Ping Chen[2] , A. K. Pandey[3], M. Tamura[4,5] , G. Maheswar[3], S. Sharma[3] ,
Jia-Wei Wang[1] , S. Nishiyama[6], Y. Nakajima[7], Jungmi Kwon[8] , R. Purcell[9,10] , and A. M. Magalhães[11]

[1] Institute of Astronomy, National Tsing Hua University, 101 Section 2, Kuang Fu Road, Hsinchu 30013, Taiwan; eswarbramha@gmail.com
[2] Institute of Astronomy, National Central University, 300 Jhongda Rd, Jhongli, Taoyuan Country 32054, Taiwan
[3] Aryabhatta Research Institute of Observational Sciences (ARIES), Manora-peak, Nainital, Uttarakhand-state, 263002, India
[4] Department of Astronomy, Graduate School of Science, The University of Tokyo, 7-3-1 Hongo, Bunkyo-ku, Tokyo 113-0033, Japan
[5] National Astronomical Observatory of Japan, 2-21-1 Osawa, Mitaka, Tokyo 181-8588, Japan
[6] Miyagi University of Education, 149 Aramaki–aza–Aoba, Aoba–ku, Sendai, Miyagi 980-0845, Japan
[7] Center of Information and Communication Technology, Hitotsubashi University, 2-1 Naka, Kunitachi, Tokyo 186-8601, Japan
[8] Institute of Space and Astronautical Science, Japan Aerospace Exploration Agency, 3-1-1 Yohinodai, Chuo-ku, Sagamihara, Kanagawa 252-5210, Japan
[9] Department of Physics and Astronomy and MQ Research Centre in Astronomy, Astrophysics and Astrophotonics, Macquarie University, NSW 2109, Australia
[10] Sydney Institute for Astronomy (SIfA), School of Physics, The University of Sydney, NSW 2006, Australia
[11] Instituto de Astronomia, Geofisica & Ciencias Atmosfericas, Universidade de São Paulo, Sao Paulo, Brazil

Abstract

The influence of magnetic fields (B-fields) on the formation and evolution of bipolar bubbles, due to the expanding ionization fronts (I-fronts) driven by the H II regions that are formed and embedded in filamentary molecular clouds, has not been well-studied yet. In addition to the anisotropic expansion of I-fronts into a filament, B-fields are expected to introduce an additional anisotropic pressure, which might favor the expansion and propagation of I-fronts forming a bipolar bubble. We present results based on near-infrared polarimetric observations toward the central $\sim 8' \times 8'$ area of the star-forming region RCW 57A, which hosts an H II region, a filament, and a bipolar bubble. Polarization measurements of 178 reddened background stars, out of the 919 detected sources in the JHK_s bands, reveal B-fields that thread perpendicularly to the filament long axis. The B-fields exhibit an hourglass morphology that closely follows the structure of the bipolar bubble. The mean B-field strength, estimated using the Chandrasekhar–Fermi method (CF method), is 91 ± 8 μG. B-field pressure dominates over turbulent and thermal pressures. Thermal pressure might act in the same orientation as the B-fields to accelerate the expansion of those I-fronts. The observed morphological correspondence among the B-fields, filament, and bipolar bubble demonstrate that the B-fields are important to the cloud contraction that formed the filament, to the gravitational collapse and star formation in it, and in feedback processes. The last one includes the formation and evolution of mid-infrared bubbles by means of B-field supported propagation and expansion of I-fronts. These may shed light on preexisting conditions favoring the formation of the massive stellar cluster in RCW 57A.

Key words: dust, extinction – ISM: magnetic fields – open clusters and associations: individual (RCW 57A) – polarization

Supporting material: machine-readable table

1. Introduction

Massive stars ($>8\,M_\odot$) have profound effects on their surrounding natal cloud material by driving strong ionizing radiation, powerful stellar winds, outflows, expanding H II regions, and supernova explosions, which either trigger or halt star formation (Beuther et al. 2002; Lee & Chen 2007; Zinnecker & Yorke 2007; Smith et al. 2010; Roccatagliata et al. 2013). Star-forming regions associated with H II regions exhibit spectacular morphologies, such as spherical or ring-like bubbles, and bipolar or unipolar bubbles (Churchwell et al. 2006, 2007; Deharveng et al. 2010; Simpson et al. 2012) that may also be surrounded by bright rimmed clouds (BRCs; Sugitani et al. 1991; Sugitani & Ogura 1994). Studies based on data from recent space missions, such as *Herschel*, *Spitzer*, and *WISE*, have shown that most molecular clouds exhibit a filamentary structure (cf., André et al. 2010;

Arzoumanian et al. 2011, 2013; Hill et al. 2011; Peretto et al. 2012; Benedettini et al. 2015) and furthermore, that they are associated with bipolar bubble-like features[12] (e.g., Minier et al. 2013; Deharveng et al. 2015; Zhang et al. 2016). Examples of molecular cloud filaments associated with bipolar/unipolar bubbles include N131 (Zhang et al. 2016), Sh 2-106 (Bally et al. 1998), IRS 16/Vela D (Strafella et al. 2010), NGC 2024 (Mezger et al. 1992), Sh 2-201 (Mampaso et al. 1987), Sh 2-88 (White & Fridlund 1992), RCW 36 (Minier et al. 2013), and RCW 57A (Minier et al. 2013).

Though bipolar bubbles are the natural outcome of the anisotropic expansion of ionizing fronts from H II regions hosting massive O/B-type star(s) located in filaments (Minier et al. 2013; Deharveng et al. 2015; Zhang et al. 2016), the details of their formation and evolution processes remain poorly understood. According to 2D (Bodenheimer et al. 1979)

---

[12] Bipolar bubbles are also referred to as hourglass-shaped nebulae, bipolar nebulae, bi-lobed appearance nebulae, and bipolar H II regions (e.g., Staude & Elsässer 1993; Minier et al. 2013; Deharveng et al. 2015).

and 3D (Fukuda & Hanawa 2000) hydrodynamic simulations, the evolution of a H II region in a filamentary cloud induces supersonic and subsonic I-fronts along the minor and major axes of the filament, respectively. This results in the distribution of low- and high-density material along the minor and major axes. Thus, the I-fronts experience more hindered flows along the major axis than along the minor axis. As a consequence of this anisotropic expansion, a bipolar bubble will be formed in the filament (Figure 1 of Deharveng et al. 2015). Though a few studies (e.g., Minier et al. 2013; Deharveng et al. 2015) were devoted to the study of bipolar bubbles, there exists no study focused on exploring the connection between the *B*-fields anchored in the filaments and their role in the formation and evolution of bipolar bubbles. Fukuda & Hanawa (2000) did include *B*-fields (parallel to the filament long axis) in their simulations, but they studied only the influence of *B*-fields on the shape, separation, and formation epoch of the cores that formed along the filament.

B-fields are believed to guide the contraction of cloud material to form filaments in molecular clouds, and thus play a crucial role in controlling cloud stability and collapse, fragmentation into cores, and internal star formation (Pereyra & Magalhães 2004; Alves et al. 2008; Li et al. 2013; Planck Collaboration et al. 2016b; Franco & Alves 2015). A few studies (e.g., Pereyra & Magalhães 2007 toward the IRAS Vela Shell and Wisniewski et al. 2007 toward the supershell NGC 2100 in the LMC) suggest the importance of *B*-fields in the dynamical evolution of the expanding shells driven by O/B-type stars. The interplay between the expansion of an ionized nebula and the influence of *B*-fields has been the subject of several studies (e.g., Kwon et al. 2010, 2011, 2015; Pavel & Clemens 2012; Santos et al. 2012, 2014; Planck Collaboration et al. 2016c). These studies hint that *B*-fields permeating through filamentary molecular clouds would also influence the expanding I-fronts or outflowing gas, which are driven from a H II region formed in the filament.

RCW 57A (also known as NGC 3576, G291.27–0.70, or IRAS 11097−6102) is a H II region associated with a filament and bipolar bubble, and is located at a distance of 2.4–2.8 kpc (Persi et al. 1994; de Pree et al. 1999). We adopt 2.4 kpc, which is within uncertainties of both the kinematic and spectroscopic determinations (see Persi et al. 1994). Figure 1 depicts the overall morphology of RCW 57A. It contains optically bright nebulosity with several dark globules and luminous arcs (Persi et al. 1994). It is one of the massive star-forming regions in the southern sky, hosting a H II region (cyan contour) embedded in a filament (white contour) from which a widely extended bipolar bubble (yellow contours) is emerging. A deeply embedded near-IR cluster, consisting of more than 130 young stellar objects (YSOs), is associated with this region (Persi et al. 1994). The observed ratios of the infrared fine-structure ionic lines (Ne II, Ar III, and S IV; Lacy et al. 1982) indicate that at least eight O7.5V stars are necessary to account for the ionization of the region. However, even these stars may not be sufficient to account for the Lyα ionizing photons inferred from radio data (Figuerêdo et al. 2002; Barbosa et al. 2003; Townsley 2009). Based on the newly discovered cluster of stars, using X-ray data, Townsley et al. (2014) suggested that an additional cluster of OB stars that were not known before might be deeply embedded. This cluster is located slightly southwest of the center of the near-IR cluster. The 10 μm map (cf., Frogel & Persson 1974) reveals the presence of five
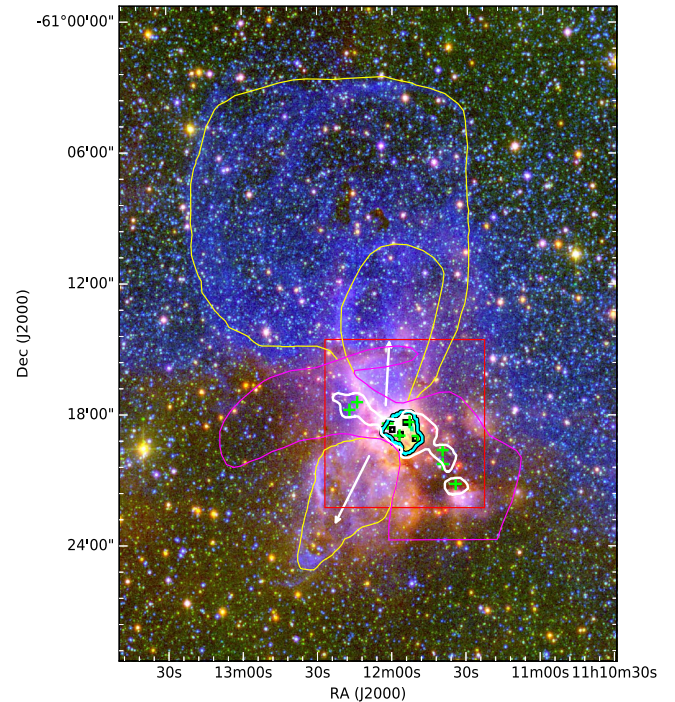

Figure 1. Tricolor image of the RCW 57A region made using *WISE* 4.6 μm (red), 2MASS K_s-band (green), and DSS2 *R*-band (blue) images. Various contours, extracted from Purcell et al. (2009), are overplotted. Yellow contours enclosing white arrows represent the bipolar bubble-like structure observed in mid-infrared (*MSX*, *Spitzer*, and *WISE*) images. This feature appears as an extended widened loop in the *R*-band, as shown with an extended yellow contour in the northern part. The thick cyan contour represents the 3.4 cm radio free–free emission from ionized gas, delimiting the extent of the H II region. The white contours represent the 1.1 mm dust continuum emission (Hill et al. 2005), showing an elongated dusty filament from northeast to southwest, which crosses the H II region. The extent of the molecular cloud, from ^{13}CO(1 − 0) line emission (Purcell et al. 2009), is depicted with the magenta outline (the horizontal line at the bottom of the magenta outline is the limit of the mapped area). IRSs (Frogel & Persson 1974) and water/methanol maser sources (cf. Purcell et al. 2009) are shown with open black squares and green crosses, respectively. The possible directions of the outflowing gas (cf. de Pree et al. 1999) are shown with white arrows. The red box denotes the area of 7′.7 × 7′.7 observed with SIRPOL.

infrared sources (IRS; black squares in Figure 1) near the center of the H II region. These, together with water and methanol maser sources (green crosses in Figure 1) distributed along the filament, are indicative of active ongoing star formation in RCW 57A (Frogel & Persson 1974; Caswell 2004; Purcell et al. 2009). Therefore, RCW 57A is an ideal target to investigate the morphological links among filaments, bipolar bubbles, and *B*-fields so as to understand the star formation history.

Here, near-infrared (NIR) polarimetric observations toward the central region of RCW 57A were carried out to map the plane-of-sky *B*-field geometry in the star-forming region. When unpolarized background starlight passes through an interstellar cloud, dust particles partially aligned by a *B*-field linearly polarize the light by a few percent. Virtually all possible mechanisms responsible for the dust grain alignment with respect to the *B*-fields (Davis & Greenstein 1951; Andersson et al. 2015; Lazarian et al. 2015) yield directions of the polarized light tracing the average *B*-field orientation projected on the plane of sky.

The aim of this paper is to understand whether (a) the *B*-field structure in the molecular cloud guides feedback processes,

such as the expansion and propagation of outflowing gas and ionization fronts, which lead to the formation of bipolar bubbles, or (b) feedback processes regulate the resulting B-field structure. The B-field is *active* in the former scenario, while it is *passive* in the latter.

The structure of this paper is as follows. Section 2 describes the observations and data reduction. Detailed analyses are presented in Section 3, the main purpose of which is to identify and remove the YSOs from the list of foreground and background stars by utilizing NIR and mid-infrared (MIR) colors, NIR polarization measurements, and polarization efficiencies. Results are presented in Section 4. This section presents estimates of the B-field strength and detailed comparisons between the B-field pressure to turbulent and thermal pressures. A possible evolutionary scenario, based on the morphological correspondences among the filament, bipolar bubble, and B-fields is discussed in Section 5. Furthermore, based on the scenario that best characterizes our observed B-fields in RCW 57A, we discuss the possible preexisting conditions that might have favored the formation of the star cluster in RCW 57A. Conclusions are summarized in Section 6.

2. Observations and Data Reduction

Simultaneous observations in the J (1.25 μm), H (1.63 μm), and K_s (2.14 μm) bands toward the central star-forming region of RCW 57A ($\alpha = 11^{\rm h}11^{\rm m}54\overset{\rm s}{.}8$, $\delta = -61°18'26''$ [J2000]) were carried out on 2007 May 6 using the imaging polarimeter SIRPOL (polarimetric mode of the Simultaneous IR Imager for Unbiased Survey, SIRIUS, camera; Kandori et al. 2006) mounted on the IR Survey Facility (IRSF) 1.4 m telescope at the South Africa Astronomical Observatory (SAAO). The SIRIUS camera was equipped with a rotating achromatic (1–2.5 μm) half-wave plate (HWP) and high extinction-ratio wire grid analyzer, three 1024 × 1024 HgCdTe (HAWAII) IR detectors, and JHK_s filters for simultaneous observations (Nagashima et al. 1999; Nagayama et al. 2003). The field of view was 7$\overset{\prime}{.}$7 × 7$\overset{\prime}{.}$7 with a pixel scale of 0$\overset{\prime\prime}{.}$45 pixel^{-1}.

One set of observations consisted of 10 s exposures at four HWP position angles (0°, 22$\overset{\circ}{.}$5, 45°, and 67$\overset{\circ}{.}$5) at 10 dithered sky pointings. Such sets of 4 × 10 images were repeated toward the same sky coordinates to increase signal-to-noise ratio (S/N). Sky frames were also obtained between target observations. The total integration time was 400 s per HWP angle. The average seeing was 1$\overset{\prime\prime}{.}$54 ($J$), 1$\overset{\prime\prime}{.}$44 ($H$) and 1$\overset{\prime\prime}{.}$31 ($K_s$).

Master flats were created by utilizing the evening and twilight flat-field frames on the same night of the observations. We processed the data using the dedicated data reduction pipeline "PYIRSF."[13] This pipeline used the raw data from the target, sky, dark, and flat-field frames as inputs. The data reduction tasks included dark subtraction, flat-field correction, median sky subtraction, frame registration, and averaging. The final products of this pipeline were the average combined four

intensity images (I_0, $I_{22.5}$, I_{45}, and $I_{67.5}$) corresponding to the four positions of the HWP.

2.1. Aperture Photometry of Point Sources

We performed aperture photometry of point-like sources on the intensity images for the HWP angles (I_0, $I_{22.5}$, I_{45}, and $I_{67.5}$) of each of the JHK_s bands using IRAF[14] and the IDL Astronomy Library (Landsman 1993). Point sources with peak intensities above 5σ (where σ is the rms uncertainty of the particular image pixel values) of the local sky background were detected using DAOFIND. Aperture photometry was performed using the PHOT task of the DAOPHOT package in IRAF. An aperture radius was chosen to be nearly the FWHM of the point-like sources, i.e., 3.4, 3.2, and 2.9 pixels in the J, H, and K_s bands, respectively. The sky annulus inner radius was set to be 10 pixels with a 5 pixel width. A source that matched in center-to-center positions to within 1 pixel radius (i.e., 2 pixel diameter equivalent to $\sim1''$) in all four HWP images was judged to be the same star.

The Stokes I intensity of each point-like source was calculated using

$$I = \frac{1}{2}(I_0 + I_{22.5} + I_{45} + I_{67.5}) \qquad (1)$$

and used to estimate its photometric magnitude. There were 401 stars found with both IRSF and 2MASS JHK_s photometric magnitude uncertainties less than 0.1 mag. These stars were used to calibrate the IRSF instrumental magnitudes and colors to the 2MASS system. Details regarding this calibration can be found in Appendix A. From the HWP images, we were able to estimate JHK_s photometric magnitudes and colors ([$J - H$] and [$H - K_s$]) for 702 stars to uncertainties of less than 0.1 mag.

2.2. Aperture Polarimetry

Polarimetry of point-like sources (aperture polarimetry) was performed on the combined intensity images at each HWP angle. Extracted intensities were used to estimate the Stokes parameters of each star using

$$Q = (I_0 - I_{45}), \qquad (2)$$

$$U = (I_{22.5} - I_{67.5}). \qquad (3)$$

The aperture and sky radii were the same as those used in the aperture photometry on the total intensity (I) images. To obtain the Stokes parameters (Q and U) in the equatorial coordinate system, an offset rotation of 105° (Kandori et al. 2006; Kusune et al. 2015) was applied. We calculated the degree of polarization P and the polarization angle θ as follows:

$$P = \frac{\sqrt{Q^2 + U^2}}{I}, \qquad (4)$$

$$\theta = \frac{1}{2}\arctan\left(\frac{U}{Q}\right). \qquad (5)$$

The errors in P and θ were also estimated by propagating the errors in the Stokes parameters according to Equations (4) and (5).

---

[13] PYIRSF package uses PYRAF, PYTHON, and C language scripts. This pipeline was used, specifically, for the reduction of NIR polarimetric data acquired with SIRPOL on IRSF and was written and compiled by Yasushi Nakajima. A detailed description of the pipeline software and their individual tasks can be found at https://sourceforge.net/projects/irsfsoftware/. PYRAF is a product of the Space Telescope Science Institute, which is operated by AURA for NASA.

[14] IRAF is distributed by the US National Optical Astronomy Observatory, which is operated by the Association of Universities for Research in Astronomy, Inc., under a cooperative agreement with the National Science Foundation.

Since the polarization degree, P, is a positive definite quantity, the derived P value tends to be overestimated, especially for low S/N cases. To correct for this bias, we calculated the de-biased P using $P_{db} = \sqrt{P^2 - \delta P^2}$ (Wardle & Kronberg 1974), where δP is the error in P. It should be noted here that, hereafter, we consider P_{db} to be P. The absolute accuracy of the offset polarization angle for SIRPOL was estimated to be less than 3° (Kandori et al. 2006). The polarization efficiencies of the wire grid polarizer are 95.5%, 96.3%, and 98.5% at the J, H, and K_s bands, respectively, and the instrumental polarization is less than 0.3% over the field of view at each band (Kandori et al. 2006). Due to these high polarization efficiencies and low instrumental polarization, no additional corrections were made to the data. To obtain the astrometric plate solutions, we matched the pixel coordinates of the detected sources and the celestial coordinates of their counterparts in the 2MASS Catalog (Skrutskie et al. 2006), and applied the *ccmap*, *ccsetwcs*, and *cctran* tasks of the IRAF *imcoords* package to the matched lists. The rms error in the returned coordinate system was $\sim 0.\!''03$. However, since the 2MASS astrometry system is limited to about $0.\!''2$, the stellar positional uncertainties should take that into account. A total of 919 stars had polarization detection in at least one band with $P/\sigma_P \geqslant 1$.

2.3. Complete Data Sample

The polarimetric data for the 919 stars were merged with the photometry of the 702 stars, and the resultant data are presented in Table 1. Star IDs are given in column 1. The photometric data of the stars—those do not have them from IRSF—are extracted from 2MASS (Skrutskie et al. 2006) and are denoted with an asterisk along with the star IDs in column 1. The coordinates, and aperture polarimetric and photometric results of each source are presented in columns 2–12. Column 13 reports our classifications of the stars, as described in Section 3 below. Although we presented all of the stellar data satisfying the $P/\sigma_P \geqslant 1$ criterion in Table 1, further analyses used only the 461 stars having H-band polarization data which satisfied the $P(H)/\sigma_{P(H)} \geqslant 2$ criterion.

Distributions of $P(H)$ versus $[H - K_s]$ and $\theta(H)$ versus $[H - K_s]$ for the 461 stars are, respectively, presented in Figures 2(a) and (b). Also shown are the histograms of $P(H)$ (Figure 2(a)), $\theta(H)$ (Figure 2(b)), and $[H - K_s]$ (Figure 2(c)). $[H - K_s]$ colors plotted in Figure 2 (also in Figures 4–6) were converted to the California Institute of Technology (CIT) system using the relations given by Carpenter (2001). The degree of polarization $P(H)$ exhibits an increasing trend with $[H - K_s]$ color. The histogram of $P(H)$ peaks at $\sim 1\%$ of polarization. The polarization angles $\theta(H)$ of the stars span the full 0°–180° range with two groups densely concentrated around $\theta(H) \simeq 60°$ and $\theta(H) \simeq 150°$. These two dominant $\theta(H)$ distributions seem to be different from the position angle of 101° corresponding to the orientation of the Galactic plane (GP) at $b = -0.\!°72$, shown with a dashed line. Moreover, these two groups of stars exhibit different distributions of $[H - K_s]$ colors and are separated by a boundary at $[H - K_s] = 0.15$ mag. Although these two groups of stars exhibit different properties of $\theta(H)$ and $[H - K_s]$ colors, they are not as clearly separated from each other in the distribution of $P(H)$.

3. Identification of YSOs and Foreground Stars

The B-field inside the molecular cloud can be probed by using the polarimetry of background stars whose light becomes differentially extinced and linearly polarized by the dust in the cloud. Hence, a sample of background stars needs to be identified among all of the stars with measured polarizations. For this purpose, we identify and exclude the following sources: YSOs (Class I, Class II, HAe/Be stars, and NIR-excess sources) based on MIR and NIR color–color diagrams, stars with L-band excess using the data from Maercker et al. (2006), stars projected against the nebulous region where their polarizations might be contaminated by scattering (especially at the cluster center), stars with non-interstellar polarization origin due to reflected light from their circumstellar disks/envelopes (whose properties cannot be discerned based on MIR and NIR colors), and the stars that have suffered depolarization effects due to multiple B-field components (associated with multiple dust layers) along their lines of sight. The latter two are identified using the polarization efficiency diagram.

Below, we present MIR and NIR two-color diagrams (TCDs) and polarization efficiency (P versus $H - K_s$) diagrams to identify and exclude the above-mentioned stars with intrinsic polarization. Finally, the remaining sample, which is free from intrinsic polarization, is subcategorized further into foreground (FG) and background (BG) stars, based on their NIR colors and polarization characteristics.

3.1. YSOs Identified by Their Mid-infrared Colors

Since the RCW 57A region is still enshrouded in its natal molecular cloud, as evident from the $^{13}CO(1-0)$ map (magenta contour in Figure 1 and red background in Figure 7), YSOs in the region can be deeply embedded. Therefore, the *Spitzer* MIR observations were used to gain deeper insight into the embedded YSOs. These occupy distinct regions in the *Spitzer* IRAC color plane, which makes MIR TCDs a useful tool for the classification of YSOs. Since 8.0 μm data are not available for the region, we used $[[K_s] - [3.6]]_0$ and $[[3.6]-[4.5]]_0$ (cf. Gutermuth et al. 2009) to identify deeply embedded YSOs, as shown in Figure 3. The zones of Class I and Class II YSOs, based on the color criteria of Gutermuth et al. (2009), are also depicted. Three sources were identified as Class I and 32 sources as Class II, and so were excluded from analyses. Identified Class I and Class II sources are mentioned in column 13 of Table 1.

3.2. YSOs Identified by Their Near-infrared Colors

NIR colors are also important tools to classify YSOs in star-forming regions. Figure 4 shows the $[J - H]$ versus $[H - K_s]$ NIR TCD for the 461 stars. The 461 stars were classified into several types as follows. The three Class I sources and 32 Class II sources identified based on the *Spitzer* MIR TCD (Figure 3) are shown as the filled and unfilled stars, respectively. Fifty-seven stars exhibiting NIR excesses, falling in the "T" and "P" regions and satisfying the relation $[J - H] < 1.69 [H - K_s]$, are shown as squares. Four stars, denoted by filled triangles, are found to have nebulous backgrounds. Twenty-eight stars, shown as open diamonds, were found to have L-band excesses (Maercker et al. 2006). Two of the stars found to be Class I also have L-band excess, and similarly, three stars found to be Class II also have L-band excess. Stars identified as having an NIR

Table 1
The JHK_s Band Polarimetric and Photometric Measurements of 1074 Stars

Star ID	R.A. (°)	Decl. (°)	$P(J)$	$P(H)$	$P(K_s)$	$\theta(J)$	$\theta(H)$	$\theta(K_s)$	J	H	K_s	Classification
	(deg)	(deg)	(%)	(%)	(%)	(deg)	(deg)	(deg)	(mag)	(mag)	(mag)	
(1)	(2)	(3)	(4)	(5)	(6)	(7)	(8)	(9)	(10)	(11)	(12)	(13)
1*	167.82417	−61.30004	⋯	⋯	1.54 ± 0.12	⋯	⋯	156.1 ± 2.2	10.926 ± 0.023	10.761 ± 0.022	10.717 ± 0.021	foreground
2*	167.82453	−61.32636	⋯	⋯	2.39 ± 0.30	⋯	⋯	56.2 ± 3.6	15.745 ± 0.125	12.896 ± 0.039	11.588 ± 0.052	background
3	167.82542	−61.25781	⋯	⋯	11.74 ± 6.92	⋯	⋯	126.7 ± 16.9	⋯	⋯	⋯	⋯
4*	167.82617	−61.28490	⋯	⋯	0.74 ± 0.38	⋯	⋯	125.6 ± 14.7	13.251 ± 0.023	12.364 ± 0.022	12.038 ± 0.024	⋯
5*	167.82662	−61.29078	⋯	⋯	3.81 ± 3.43	⋯	⋯	135.5 ± 25.8	14.972 ± 0.033	14.590 ± 0.045	14.632 ± 0.101	⋯
6	167.82681	−61.27721	⋯	⋯	⋯	⋯	⋯	⋯	15.709 ± 0.069	14.958 ± 0.054	14.705 ± 0.062	⋯
7	167.82700	−61.27257	⋯	⋯	⋯	⋯	⋯	⋯	15.670 ± 0.051	14.537 ± 0.032	14.029 ± 0.031	⋯
8	167.82750	−61.27381	2.12 ± 0.07	1.16 ± 0.04	1.31 ± 0.05	39.0 ± 0.9	66.3 ± 0.9	81.9 ± 1.1	11.136 ± 0.006	10.148 ± 0.004	9.792 ± 0.003	background
9*	167.82789	−61.24061	⋯	2.26 ± 0.90	2.13 ± 1.23	⋯	81.9 ± 11.4	84.8 ± 16.5	14.924 ± 0.043	13.789 ± 0.029	13.331 ± 0.034	background
10	167.82793	−61.28848	⋯	⋯	8.42 ± 3.82	⋯	⋯	38.7 ± 13.0	15.629 ± 0.031	14.989 ± 0.022	14.852 ± 0.035	foreground†
11*	167.82798	−61.35974	⋯	9.91 ± 3.27	8.22 ± 3.22	⋯	99.8 ± 9.5	78.8 ± 11.2	17.096	15.273 ± 0.079	14.257 ± 0.078	background
12*	167.82850	−61.31453	⋯	1.67 ± 1.12	⋯	⋯	66.7 ± 19.1	⋯	14.636 ± 0.036	14.248 ± 0.038	14.155 ± 0.063	⋯
13	167.82881	−61.27652	⋯	⋯	3.63 ± 1.94	⋯	⋯	97.7 ± 15.3	15.635 ± 0.044	14.374 ± 0.021	13.893 ± 0.021	⋯
14	167.82915	−61.30585	2.31 ± 1.76	⋯	⋯	53.0 ± 21.8	⋯	⋯	14.992 ± 0.020	14.057 ± 0.013	13.766 ± 0.016	⋯
15*	167.82931	−61.32771	⋯	⋯	6.63 ± 2.74	⋯	⋯	55.5 ± 11.8	16.722	15.578 ± 0.164	14.359 ± 0.085	Class II
16	167.82960	−61.27960	5.00 ± 2.67	2.39 ± 1.98	⋯	30.7 ± 15.3	92.2 ± 23.6	⋯	15.393 ± 0.028	14.823 ± 0.022	14.533 ± 0.029	⋯
17*	167.82972	−61.31241	⋯	2.37 ± 1.04	3.43 ± 1.48	⋯	100.6 ± 12.6	89.2 ± 12.4	15.828 ± 0.081	14.321 ± 0.055	13.752 ± 0.058	background
18	167.83039	−61.33665	⋯	1.11 ± 0.70	3.20 ± 0.75	⋯	79.4 ± 18.1	144.0 ± 6.7	14.869 ± 0.019	13.172 ± 0.009	12.342 ± 0.009	⋯
19*	167.83094	−61.23723	⋯	6.24 ± 3.39	⋯	⋯	97.2 ± 15.5	⋯	14.870 ± 0.101	14.560 ± 0.114	14.444 ± 0.124	⋯
20	167.83131	−61.33597	3.37 ± 0.13	4.04 ± 0.04	1.46 ± 0.04	86.4 ± 1.1	85.6 ± 0.3	84.6 ± 0.7	12.434 ± 0.009	10.229 ± 0.003	9.275 ± 0.005	background

Notes.

Star IDs marked with a ⋆ denotes that their photometric data taken from 2MASS (Skrutskie et al. 2006).

The polarization values given in columns 4–6 are de-biased.

The uncertainties in the polarization angles given in columns 7–9 do not account for the overall angular calibration uncertainty of 3°, which is a systematic uncertainty that would affect all of the measured polarization angles.

Column 13: "Foreground" means confirmed foreground stars.

Column 13: "Background" means confirmed background stars or cluster members.

Column 13: "Foreground†" means probable foreground stars with $P(H) > 3\%$ (see Section 3.3).

Column 13: "Background††" means probable background stars or cluster member with excess polarization (see Section 3.3).

Column 13: "Background‡" means probable background star or cluster member with depolarization (see Section 3.3).

The entries that do not have 2MASS photometric uncertainties are left blank

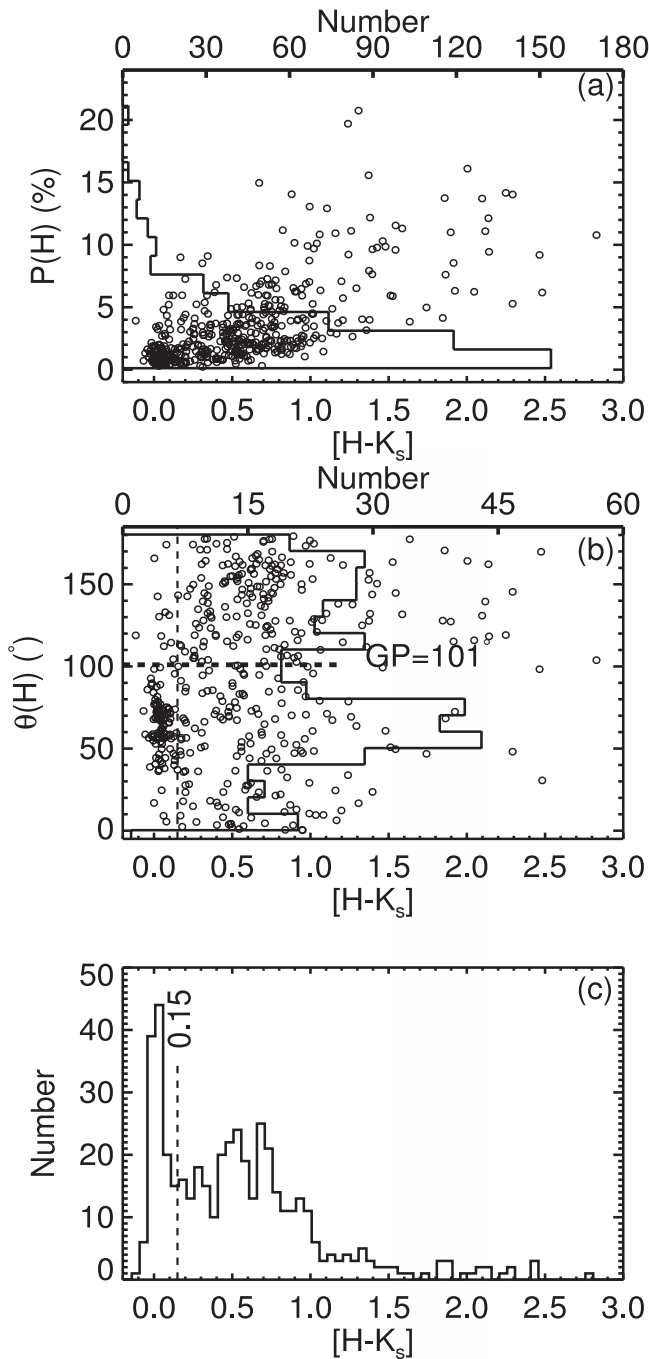(This table is available in its entirety in machine-readable form.)

Figure 2. (a) $P(H)$ and (b) $\theta(H)$ vs. $[H - K_s]$ color for 461 stars. The histograms of (a) $P(H)$, (b) $\theta(H)$, and (c) $[H - K_s]$ are also shown.
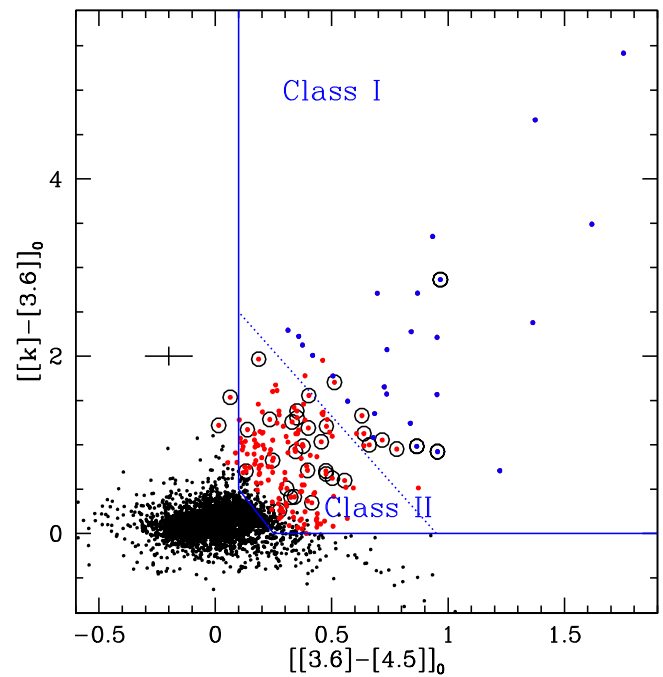

Figure 3. $[[K_s] - [3.6]]_0$ vs. $[[3.6]-[4.5]]_0$ TCD (two-color diagram) for the *Spitzer* IRAC sources. Black dots are the total sample in the entire region. The blue and red filled circles represent Class I and Class II sources, respectively, in the RCW 57A region. The black circles surrounding some of the points are the three Class I and 32 Class II sources having 2σ polarization measurements. The slanted dotted line denotes the boundary between Class I and Class II YSOs. The average error in the colors is shown.

Williams 2005; Cieza et al. 2007). Therefore, it is reasonable to assume that these WTTSs are not intrinsically polarized by scattered light from the negligible amount of circumstellar material.

In order to estimate the level of FG contamination, a control field ($\alpha = 11^h18^m12^s.22$, $\delta = -61°59'38''.92$ [J2000]) of angular size $7'.7 \times 7'.7$ located $\sim60'$ from the RCW 57A region was chosen. Comparing the distributions of the $[H - K_s]$ colors of the control field with colors in the RCW 57A region shows the field stars to have $[H - K_s] < 0.15$. Therefore, the 108 RCW 57A stars with $[H - K_s] < 0.15$ and lying in the "F" region of the NIR TCD are judged to be FG star candidates, and the remaining 234 stars with $[H - K_s] \geqslant 0.15$ and lying in the "F" region are judged to be BG star candidates.

3.3. Final Confirmed FG and BG Stars Based on Polarization Efficiency Diagrams

Polarization efficiency is defined as the ratio of polarization degree to interstellar reddening, such as $P(\lambda)/E(\lambda_1 - \lambda_2)$. Observed polarization efficiencies of dust grains are found to vary from one line of sight to another. Reddening ($E(B - V)$) and polarization in the V-band (P_V) are correlated and can be represented by the observational upper limit relation: $P_V/E(B - V) \leqslant 9\%$ mag^{-1} (Serkowski et al. 1975). Polarization measurements that exceed this upper limit relation are generally attributed to the intrinsic polarization (non-magnetic polarization) caused by scattered light from dust grains in circumstellar disks or envelopes around YSOs (e.g., Kandori et al. 2007; Eswaraiah et al. 2011, 2012; Serón Navarrete et al. 2016).
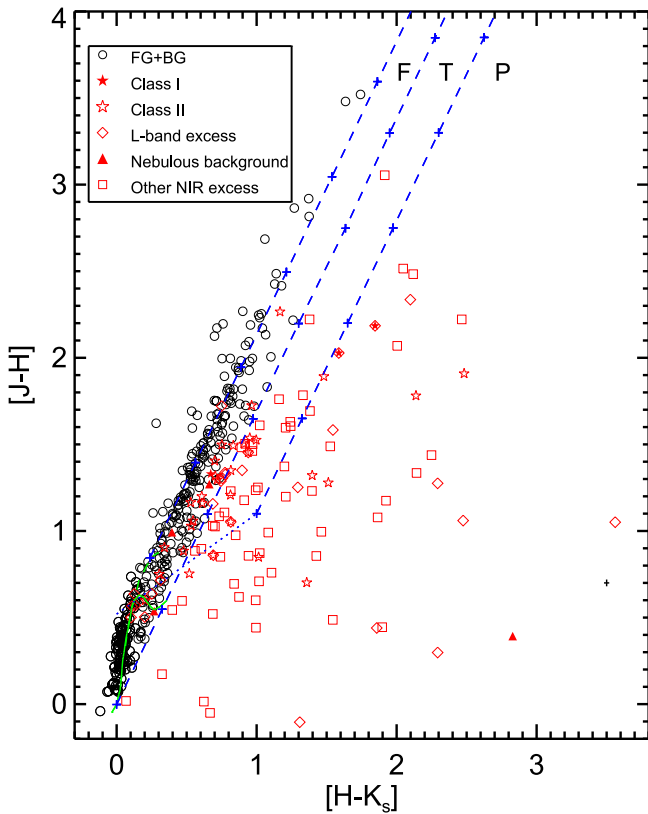
excess, L-band excess, and a nebulous background are noted in column 13 of Table 1.

The remaining 342 stars that appear to be free from intrinsic polarization and are distributed in zone "F" in Figure 4 are (i) lightly reddened foreground field stars (FG stars), (ii) moderately reddened cluster members and highly reddened background stars (hereafter, both cluster members and background stars are referred to as BG stars), and (iii) weak line T-Tauri stars (WTTSs) or Class III sources. The locations of the WTTSs in the NIR TCD overlap with those of the reddened background stars. Generally, WTTSs exhibit almost negligible NIR excess, as their disks will have been evaporated already or be very optically thin (e.g., Adams et al. 1987; Andrews &

Figure 4. $[J - H]$ vs. $[H - K_s]$ NIR TCD (two-color diagram) for the 461 star sample. The continuous and dashed green curves represent the unreddened MS and giant branch (Bessell & Brett 1988), respectively. The dotted blue line indicates the locus of unreddened CTTSs. The parallel blue dashed lines are the reddening vectors drawn from the tip (spectral type M4) of the giant branch (left reddening line), from the base (spectral type A0) of the MS branch (middle reddening line), and from the tip of the intrinsic CTTS line (right reddening line) with the extinction ratios $A_J/A_V = 0.265$, $A_H/A_V = 0.155$, and $A_K/A_V = 0.090$ (Cohen et al. 1981). The blue plus symbols on the reddening vectors show increments of A_V by 5 mag each. The sources located in the "F" region could be either reddened field stars or Class II and Class III sources with small NIR excesses. The sources distributed in the "T" and "P" regions are considered to be mostly Classical T-Tauri stars (CTTSs; Meyer et al. 1997) or Class II sources with relatively large NIR excesses and likely Class I sources, respectively (for details, see Pandey et al. 2008; Chauhan et al. 2011a, 2011b). Typical errors, shown with a plus symbol in the bottom right of the plot, are small and are comparable to the sizes of the symbols.

We also seek to identify and exclude the stars that suffer depolarization due to their starlight passing through multiple *B*-field components along the line of sight. For optically thin clouds, $P(\lambda)$ is expected to be proportional to the column density if the field structure is uniform. In contrast, the presence of multiple *B*-fields with different orientations along a line of sight will result in depolarization (Martin 1974) and hence weaken the correlation between polarization and extinction (e.g., Eswaraiah et al. 2011, 2012). Therefore, polarization efficiency diagrams (e.g., Kwon et al. 2011; Sugitani et al. 2011; Hatano et al. 2013) will help identify stars with either intrinsic polarization or depolarization.

Figure 5 shows the *P* versus $[H - K_s]$ diagrams of FG and BG candidate stars (Section 3.2) with *H*-band data. These diagrams contain no known YSOs as we excluded them in Sections 3.1 and 3.2. The BG candidate stars show an increasing trend in polarization in accordance with an increasing $[H - K_s]$ and are well distributed below the
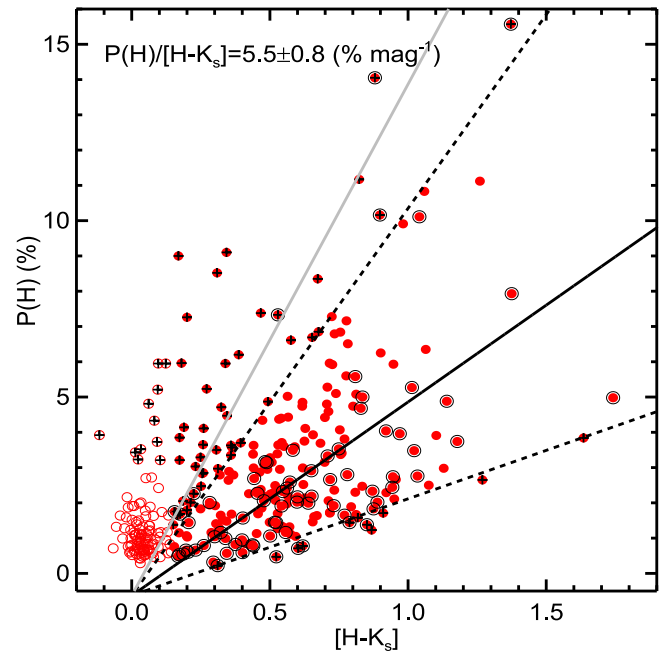

Figure 5. Polarization efficiency in the *H*-band. $P(H)$ vs. $[H - K_s]$ for 108 FG candidate (open red circles) and 234 BG candidate (filled red circles) stars. Encircled red filled circles correspond to the 76 BG candidate stars with $\sigma_{P(H)} < 0.3\%$. A linear fit (solid lines) was made to these encircled stars, and the slope and uncertainty are quoted. The dashed lines are drawn with slopes twice and half of the slope that correspond to the solid lines. The plus symbols overlaid on the unfilled and filled circles are the stars excluded from the list of confirmed FG and BG stars. The gray line in each panel represents the upper limit polarization efficiency relation corresponding to $P(V)/E(B - V) \leqslant 9\%$ mag^{-1} (Serkowski et al. 1975).

upper limit interstellar polarization efficiency relation (gray line), $P(H)/E(H - K_s) = 14.5\%$ mag^{-1}, corresponding to $P(V)/E(B - V) = 9\%$ mag^{-1} (Serkowski et al. 1975; also see Hatano et al. 2013 for a detailed description on deriving polarization efficiency relations in NIR wavelengths.). To find the stars with non-magnetic polarizations (non-interstellar origin of polarizations) and depolarization effects, first, we fit a straight line to the polarization versus extinction for BG stars with $\sigma_{P(H)} < 0.3\%$ (encircled filled circles). Second, we drew dashed lines with slopes of twice (upper dashed line) and half (lower dashed line) the fitted slopes. Third, we identified the stars falling above and below these lines as probable BG stars that were influenced by the non-magnetic origin of the polarization and depolarization effects, respectively. The remaining stars falling between the two dashed lines are ascertained to be confirmed BG stars. Therefore, the final number of confirmed BG stars was found to be 178 in the *H*-band. An additional 64 candidate BG stars falling above and below the dashed lines (plus symbols) are mentioned as probable BG stars with intrinsic polarization or depolarization in Table 1.

FG candidate stars (open circles) exhibit two distributions and those with $P(H) > 3\%$ (plus symbols on open circles) may be affected by additional polarization caused by scattering or simply by larger uncertainties. We consider them to be probable FG stars. The remaining 97 stars with $P(H) \leqslant 3\%$ are considered to be confirmed FG stars in the *H*-band. These confirmed and probable FG stars are mentioned in Table 1.

In further analysis, we only used the confirmed 97 FG and 178 BG stars with *H*-band data. The fitted slope of

$P(H)/E(H - K_s) = 5.5\% \pm 0.8\%\,\mathrm{mag}^{-1}$ (thick line) suggests that the polarization efficiency of dust grains in the star-forming cloud RCW 57A are relatively higher than those of other Galactic lines of sight (e.g., Hatano et al. 2013; Kusune et al. 2015).

4. Results

4.1. Separation of Foreground and Background Magnetic Fields

FG stars toward any distant cluster are, generally, less polarized and extincted than BG stars (Eswaraiah et al. 2011, 2012; Pandey et al. 2013). This is because the dust layer(s) between the observer and the FG star contains fewer aligned dust grains, and because the degree of polarization and extinction are linearly correlated (Aannestad & Purcell 1973; Serkowski et al. 1975; Hatano et al. 2013). If the B-field orientation of the foreground dust layer is sufficiently different from that of the cloud, then FG stars would exhibit different polarizations (P and θ) from BG stars. Therefore, FG and BG stars can also be distinguished based on their polarization characteristics (P versus θ or Q versus U), as well as with their NIR colors (Medhi et al. 2008, 2010; Eswaraiah et al. 2011, 2012; Medhi & Tamura 2013; Pandey et al. 2013; Santos et al. 2014).

Figures 6(a)–(d) depict that the 97 confirmed FG and 178 confirmed BG stars are well separated in their polarization characteristics and $[H - K_s]$ colors. FG stars have $[H - K_s] < 0.15$, $P(H) < 3\%$ with a peak around 1.0% and a single Gaussian distribution of $\theta(H)$ (Gaussian mean of 65° with a standard deviation of 14°). BG stars have $[H - K_s] \geqslant 0.15$, $P(H)$ between 0.5%–12% with a peak at $\sim 2\%$, and an extended tail toward greater P values and widely distributed $\theta(H)$ (ranging from 0° to 180°) indicating the presence of a complex B-field structure in RCW 57A with a prominent peak at $\theta(H) \sim 163°$. About 55% of stars are distributed between 110° and 180°, whereas the remaining 45% of stars are distributed between 0° and 110°. This suggests that the plane-of-sky B-field structure of RCW 57A is dominated by a component with $\theta(H) \sim 163°$, which is nearly orthogonal to the foreground B-field component (65°) as well as being nearly orthogonal to the position angle of the major axis of the filament ($\sim 60°$). Figure 6(d) also reveals that the distributions of $\theta(H)$ of the confirmed FG and BG stars are different from the position angle (101°) of the Galactic plane (GP) at $b = -0°.72$, shown with a thick vertical line.

4.2. B-field Structure toward RCW 57A

4.2.1. Contribution of Foreground Polarization

In order to account for the influence of foreground (FG) polarization on the polarization angles of the confirmed BG stars, below we performed FG subtraction. First, the polarization measurements of the 97 confirmed FG stars were converted into Stokes parameters. Second, the weighted-mean FG Stokes parameters were computed and found to be $Q_{\mathrm{FG}} = -0.332\% \pm 0.008\%$ and $U_{\mathrm{FG}} = 0.845\% \pm 0.007\%$ (with a standard deviation of 0.64% in Q_{FG} and 0.70% in U_{FG}) and were subtracted vectorially from those of each confirmed BG star. Third, FG-subtracted Stokes parameters of the BG stars were then converted back to $\theta(H)_{\mathrm{FG\text{-}corrected}}$.

The Gaussian mean and standard deviation, for the distribution of offset polarization angles of the BG stars ($\theta(H) - \theta(H)_{\mathrm{FG\text{-}corrected}}$), are found to be 1° and 7°, respectively. Hence, there was no obvious change in the FG-corrected B-field morphology inferred from the BG stars. Therefore, we ignored the FG contribution to the BG polarization measurements.

4.2.2. Magnetic Field Geometry

Figure 7 shows the vector map of the H-band polarization measurements of the 178 confirmed BG stars. The polarization vector map reveals a systematically ordered B-field that is configured into an hourglass morphology closely resembling the structure of the bipolar bubble.

The direction of the expanding I-fronts or outflowing gas is revealed based on a large north–south velocity gradient in radio recombination line observations (de Pree et al. 1999). These high-velocity outflow signatures are further traced in $^{13}\mathrm{CO}(1-0)$ position–velocity (P–V) diagrams (Figure 11; shown below). Shocked gas is visible at the SE and NW ends of the white arrows in Figure 7 (also see Figure 1), highlighting the outflow–cloud interaction. Townsley et al. (2011, see their Figures 3 and 4) have also showed that outflows from the deeply embedded protostars are responsible for the soft X-ray emission observed in the SE part of the cloud. These outflows have created the cavities depicted by the enclosed yellow contours (Figure 1). Interestingly, the directions of the expanding I-fronts and/or outflowing gas, as depicted by the white arrows (Figure 7), follow the B-field orientations.

B-fields are compressed along the rim of the BRC (located inside the white box in Figure 7); more details on these are addressed in Appendix B.

4.3. Extracting Essential Parameters for Estimating Magnetic Field Strength

To test whether B-fields play an active role in the formation of bipolar bubbles, it is essential to estimate the B-field strength by using the Chandrasekhar & Fermi (1953) relation (the CF method). For this purpose, below we determine the dispersion in $\theta(H)$ for the BG stars, the gas velocity dispersion using CO data, and the dust and gas volume density using *Herschel* data.

4.3.1. Dispersion in Polarization Angles: $\sigma_{\theta(H)}$

The presence of multiple components of B-fields in RCW 57A can be seen from the H-band polarization vector map overlaid on the $^{13}\mathrm{CO}(1-0)$ (Purcell et al. 2009) total integrated intensity image (Figure 8) and the histogram of $\theta(H)$ (continuous histogram in Figure 6(d)). Each component follows its own spatial distribution and exhibits its own $\theta(H)$ distribution and dispersion. For this reason, we divided the observed area into five regions, named A, B, C, D, and E, as shown in Figure 8 and Table 2. The spatial extent of each region is visually chosen in such a way that it should not include multiple components of $\theta(H)$. This criterion constrains the dispersion of $\theta(H)$ to be less than 25° (Ostriker et al. 2001) in order to apply the CF method to estimate the B-field strength. Some portions are not included because they either have polarization data but not CO data (the area to the right of the C region), or have CO data but multiple $\theta(H)$ distributions (area slightly above the E region), or they contain few randomly
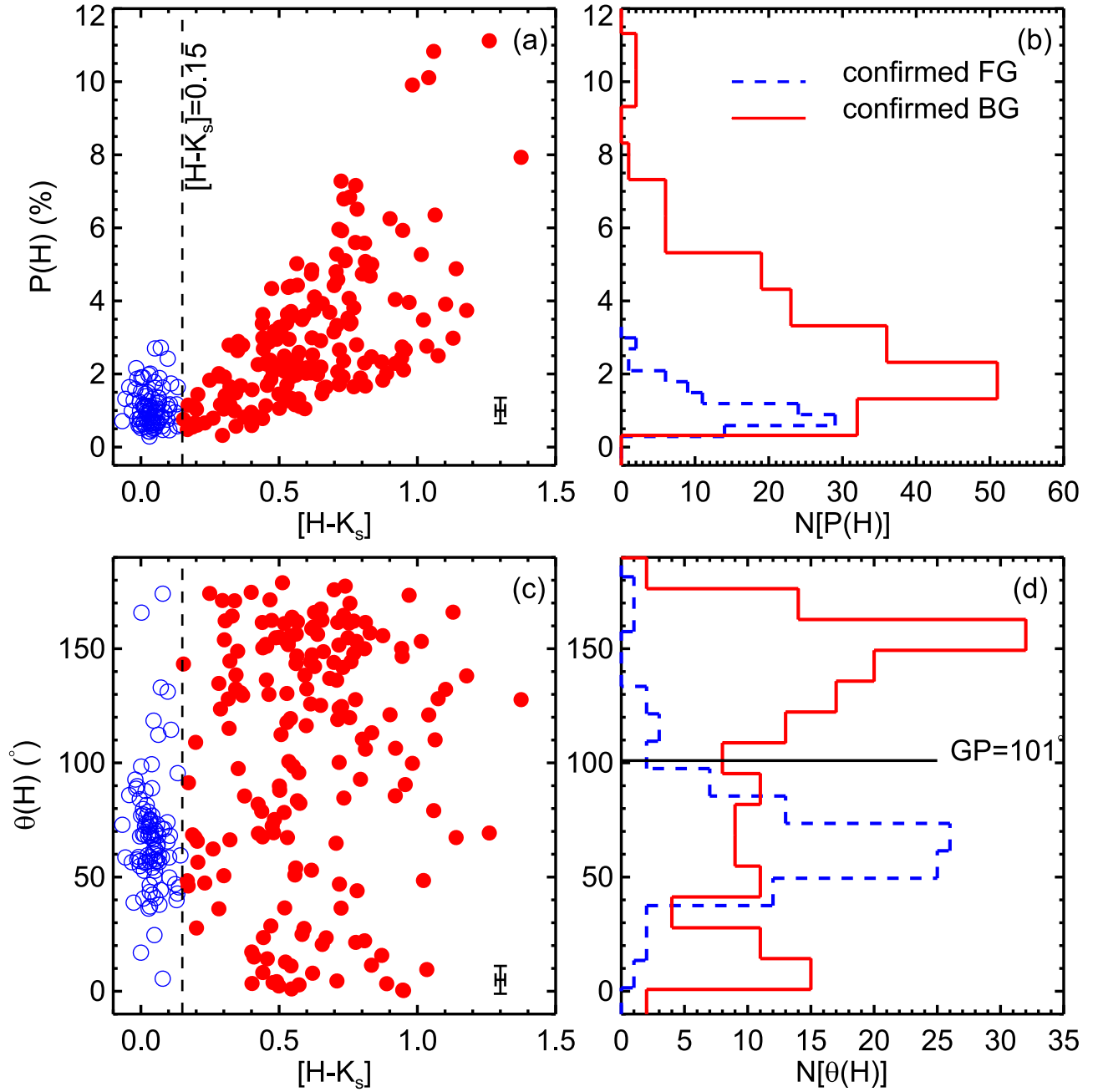
Figure 6. Polarization properties of confirmed FG and BG stars. (a) $P(H)$ vs. $[H - K_s]$ for the 97 confirmed FG stars (unfilled blue circles) and 178 confirmed BG stars (filled red circles). (c) Same as (a) but for $\theta(H)$ vs. $[H - K_s]$. The dashed line drawn at $[H - K_s] = 0.15$, in (a) and (c), separates FG and BG stars. Typical errors are plotted at the bottom-right corner of (a) and (c). (b) Distributions $P(H)$ for the 97 confirmed FG (dashed histogram) and 178 confirmed BG (continuous histogram) stars as plotted in (a) and (c). (d) Same as (b) but for $\theta(H)$.

oriented vectors (area distributed between the D and E regions). We believe that the bias involved in the selection of the five regions may not have significant impact on the final scientific results.

A Gaussian function was fit to the $\theta(H)$ distribution for each region, as shown in Figure 9. The fitted means and dispersions in polarization angles, along with their errors, are listed in columns 7 and 8 of Table 2, respectively. The mean $\theta(H)(=\mu_{\theta(H)})$ values of regions A, B, C, D, and E are found to be 26°, 164°, 153°, 132°, and 74°, respectively. Dispersions in the $\theta(H)$ ($=\sigma_{\theta(H)}$) of the five regions lie between 10° and 16°.

4.3.2. Velocity Dispersion: $\sigma_{V_{LSR}}$

To derive the velocity dispersion in regions A, B, C, D, and E, we used $^{13}CO(1-0)$ emission line mapping (Figure 8) performed using the *Mopra* telescope by Purcell et al. (2009). The observed $^{13}CO(1-0)$ data have a velocity resolution of 0.4 km s^{-1} and a spatial resolution of 40″. CASA software was used to extract the mean velocity (V_{LSR}) versus brightness temperature (T) spectrum of each region, which is plotted in Figure 10 using small filled circles. All of the regions exhibit at least two velocity components, with clear asymmetric spectra toward higher velocities. These asymmetric, spatially extended
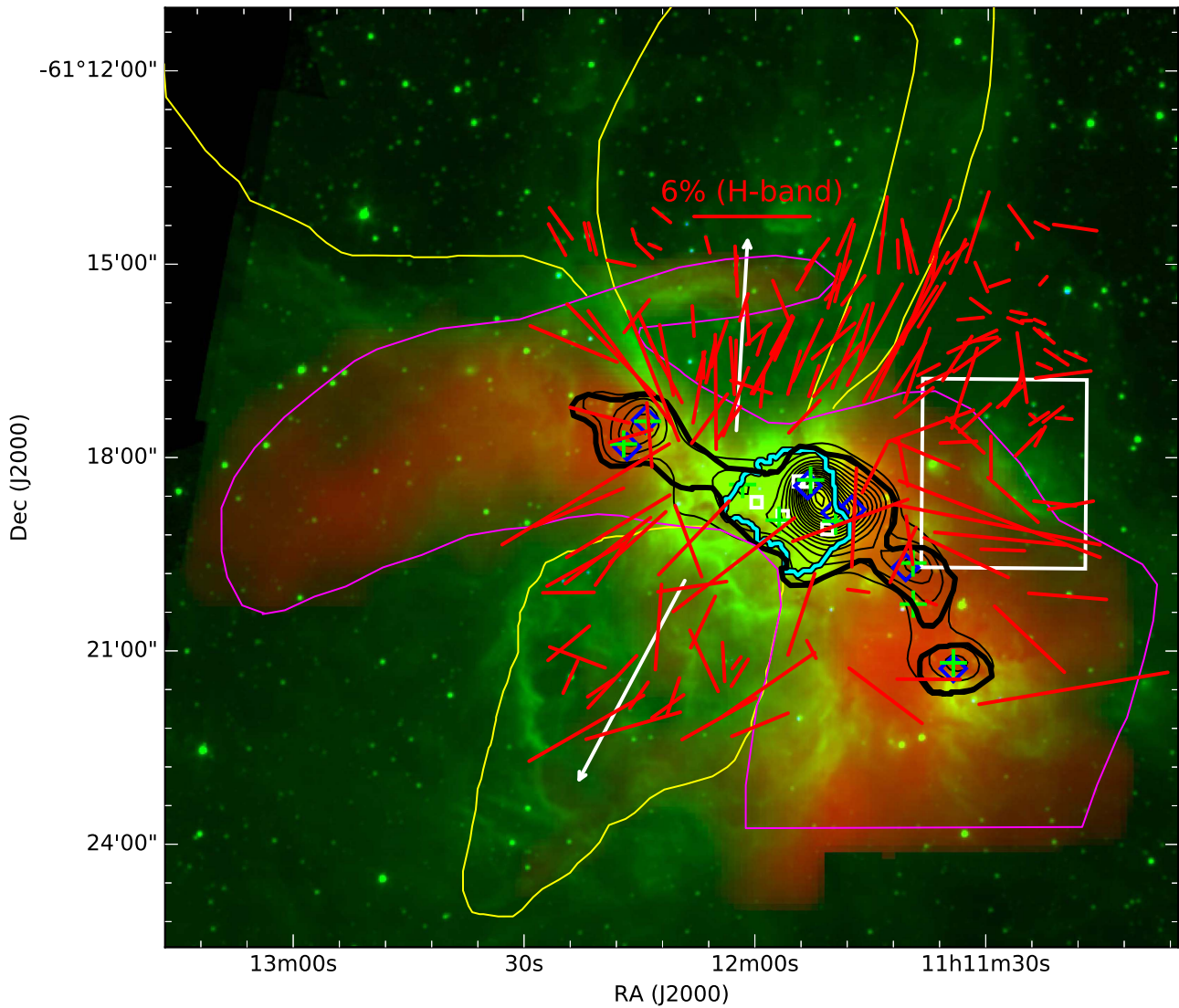
Figure 7. *H*-band polarizations (red vectors) of the 178 confirmed BG stars overlaid on the tricolor image constructed from the ^{13}CO$(1-0)$ total integrated emission map (red; Purcell et al. 2009), *Spitzer* IRAC Ch2+Ch3 combined image (green), and SIRPOL $J + H + K_s$ band combined image (blue). Reference vector with $P = 6\%$ and $\theta = 90°$ is plotted. The thick black contour represents SIMBA 1.2 mm dust emission (Hill et al. 2005) with a flux level of $\sim$3 Jy beam^{-1}. The thin black contours denote ATLASGAL 0.87 mm thermal dust emission ranging from 2 Jy beam^{-1} to 22 Jy beam^{-1} (beam size of 18″2) with an interval of 1 Jy beam^{-1}. The cyan contour represents the extent of the H II region, as traced in 3.4 cm radio free–free emission (de Pree et al. 1999). Yellow contours delineate the morphology of the bipolar bubble. The magenta contour depicts the extent of the molecular cloud, as traced by ^{13}CO$(1-0)$ emission using the *Mopra* telescope (Purcell et al. 2009). The white box shows the location of a bright rimmed cloud. White arrows represent possible orientations of expanding I-fronts or outflowing gas. The green plus marks and black squares distributed along the filament are the water/methanol masers and IRSs, respectively. Blue diamonds correspond to the seven massive cores (namely, S1–M1, S1–M2, S3–M4, S3–M5, S3–C3, S4–M6, and S5–M6) identified by André et al. (2008). All of the information on various contours, and the location of the masers and IRSs is extracted from Purcell et al. (2009), by permission.

spectra correspond to outflowing gas from the embedded YSOs, expanding I-fronts, or both. Each of these spectra (*T* versus V_{LSR}) were then fitted by a multi-Gaussian function using the custom IDL routine "gatorplot.pro."[15] Details regarding this multi-Gaussian fitting are described in Appendix C.

The resulting multi-Gaussian fitting parameters of each spectrum are presented in Table 3 and plotted with black lines in Figure 10. The resulting combined spectrum of each region, the sum of all fitted multi-Gaussians (orange line), closely match the observed spectrum. The difference between the observed and fitted spectra, the residuals, are shown with open squares and are closely distributed around zero *T*. Among the

multiple velocity components of each region, we attribute the one related to the peak of the spectrum to the turbulent cloud component of that region (red Gaussian curve). These are used to estimate the *B*-field strength. The remaining Gaussian velocity components (black lines) are ascribed to the expanding I-fronts and outflowing gas. These values are also given in column 9 of Table 2.

The dashed line drawn at $V_{\mathrm{LSR}} = -26.5$ km s^{-1} (Figure 10) corresponds to the line center velocity over the areas covered by regions A, B, C, and D of RCW 57A. This $V_{\mathrm{LSR}} = -26.5$ km s^{-1} component closely matches the center of the red Gaussian components of all regions, except for region E. However, based on the dense gas tracers (NH$_3$, N$_2$H$^+$, and CS), Purcell et al. (2009) witnessed that the peak

---

[15] http://www.astro.ufl.edu/~warner/GatorPlot/

Table 2
Central Coordinates, Widths, Number of Stars, Mean ($\mu_{\theta(H)}$) and Dispersion ($\sigma_{\theta(H)}$) in Polarization Angles (Using Gaussian Fitting), Velocity Dispersion ($\sigma_{V_{LSR}}$) Using ^{13}CO(1 − 0) Data, Volume Density ($n(H_2)$) Using *Herschel* Data and Plummer-like Profile Fitting on Column Density Maps, and Magnetic Field Strength Estimated using the Chandrasekhar–Fermi Method for Regions A, B, C, D and E

Region (1)	R.A. (J2000) (deg) (2)	Decl. (J2000) (deg) (3)	Width in R.A. (arcmin) (4)	Width in Decl. (arcmin) (5)	No. of Stars (6)	$\mu_{\theta(H)}$ (deg) (7)	$\sigma_{\theta(H)}$ (deg) (8)	$\sigma_{V_{LSR}}$ (km s^{-1}) (9)	$n(H_2)$ ($\times 10^3$ cm^{-3}) (10)	B (CF)[a] (μG) (11)	B (CF)[b] (μG) (12)
A	168.0640	−61.2732	1.35	1.87	7	26 ± 6	10 ± 7	0.8 ± 0.1	5.15 ± 0.68	123 ± 89	123 ± 21
B	168.0088	−61.2763	1.76	2.24	24	164 ± 3	16 ± 3	1.1 ± 0.1	3.51 ± 0.41	89 ± 21	89 ± 13
C	167.9485	−61.2594	1.65	2.54	20	153 ± 2	11 ± 3	1.0 ± 0.2	1.01 ± 0.09	63 ± 23	63 ± 15
D	168.0562	−61.3415	2.99	3.48	27	132 ± 2	14 ± 3	1.4 ± 0.3	2.52 ± 0.21	108 ± 36	108 ± 27
E	167.8658	−61.3180	1.53	1.53	6	74 ± 6	15 ± 10	0.9 ± 0.1	3.33 ± 0.52	74 ± 50	74 ± 8

Notes.
[a] Errors in *B*-field strengths were estimated by propagating uncertainties in $n(H_2)$, $\sigma_{\theta(H)}$, and $\sigma_{V_{LSR}}$.
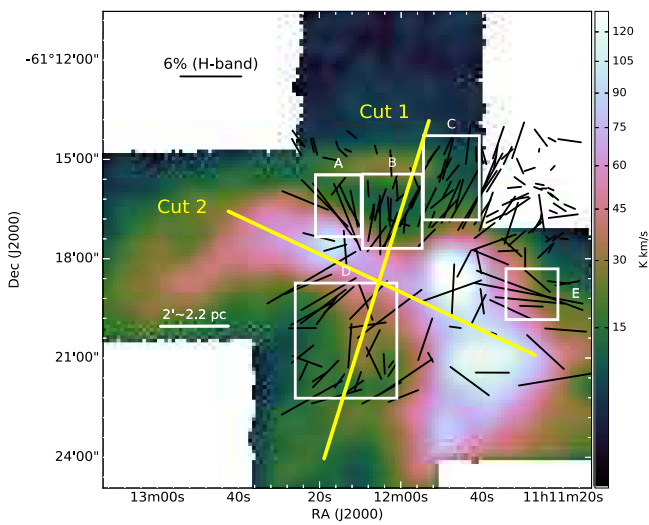[b] Errors in *B*-field strengths were estimated by propagating uncertainties only in $n(H_2)$ and $\sigma_{V_{LSR}}$.

Figure 8. *H*-band polarization vectors (black lines) of confirmed BG stars overlaid on the ^{13}CO(1 − 0) (Purcell et al. 2009) total integrated intensity image. The units of the color scale are K km s^{-1}. The white boxes, identified as A, B, C, D, and E, are the five regions selected for estimating the dispersions in gas velocity and $\theta(H)$. The thick yellow lines represent "Cut 1" and "Cut 2" along the ionization front or outflowing gas and the cloud main axis, respectively, as described in the text and used as the basis for Figure 11. A reference length scale with 2′ corresponding to 2.2 pc is shown as the horizontal white, labeled line.

V_{LSR} of the filament remained constant around −24 km s^{-1} (see their Figure 13), which is slightly different from $V_{LSR} = -26.5$ km s^{-1}. This is mainly because of the following reasons: (a) CO is optically thick and hence traces the less dense outer parts of the cloud and (b) the regions A, B, C, and D, located slightly away from the cloud center, contain less dense gas that is influenced by the H II region.

Below, we try to resolve and quantify the contributions from the turbulent cloud component, outflowing gas, and expanding I-front using *P–V* diagrams. *P–V* diagrams are useful diagnostics of gas kinematics in star-forming molecular clouds (e.g., Purcell et al. 2009; Zhang et al. 2016). Figures 11(a) and (b) show the *P–V* diagrams corresponding to the two cuts shown and labeled "1" and "2," respectively, in Figure 8. Cut "1" is along the orientation of the expanding I-front or

outflowing gas (parallel to the minor axis of the filament), and cut "2" is along the major axis of the filament.

The velocity range over the whole region, based on the extent of the contours shown in Figures 11(a) and (b), spans $\simeq -28.5$ to $\simeq -16.5$ km s^{-1} with width $\Delta V \simeq 12$ km s^{-1}. This implies that the entire region is dynamically active under the influence of the H II region. However, among all parts of the cloud that we observed, one of the most quiescent clumps, S4 (André et al. 2008; Purcell et al. 2009), is situated to the SE of the filament. This clump is situated at $\sim 250''$ and at ~ -26.5 km s^{-1} in Figure 11(b). The dust temperature T_d (~ 19–24 K; André et al. 2008) and kinetic temperature T_k (~ 15–25 K; Purcell et al. 2009) of the cores in S4 suggest that this clump is dynamically quiescent as it is far from the H II region. The gas velocity around this clump spans over ~ -25 to ~ -28 km s^{-1} (centered at ~ -26.5 km s^{-1}) and a width of 2–3 km s^{-1} (Figure 11(b)). Therefore, this velocity component at ~ -26.5 km s^{-1} is considered the cloud V_{LSR} component. Turbulent velocity dispersions of the A, B, C, D, and E regions also lie in the similar range of 2–3 km s^{-1} as noted in Table 3. According to the collect and collapse model of triggered star formation (see Torii et al. 2015 and references therein), the velocity separation due to the expanding I-front based on the *P–V* diagrams is ~ 4 km s^{-1}. Therefore, the outflowing gas may have a remaining contribution of ~ 5–6 km s^{-1} in addition to the cloud turbulent component of ~ 2–3 km s^{-1}.

Below, we decompose the relative contributions of the various velocity components in each region. In Figure 11(a), there exist two prominent redshifted, high-velocity components with peak intensities at $\simeq -20$ km s^{-1} and $\simeq -23$ km s^{-1}. These components are concentrated close to the cloud center. While the former component is attributed to the outflowing gas, the latter is attributed to the expanding I-front. The signatures of both components prevail in the A, B, C, and D regions. However, as shown in the bottom panel of Figure 10, the E region seems to be less influenced by the above two components, but it has two other prominent components: (a) ~ -25 km s^{-1}, related to the expanding I-front, and (b) ~ -23 km s^{-1}, attributed to the turbulent cloud region. Moreover, spatially, the E region, in comparison to the others, is located far from the area influenced by the outflowing gas as depicted by the white arrows (cf. Figure 7). This implies that
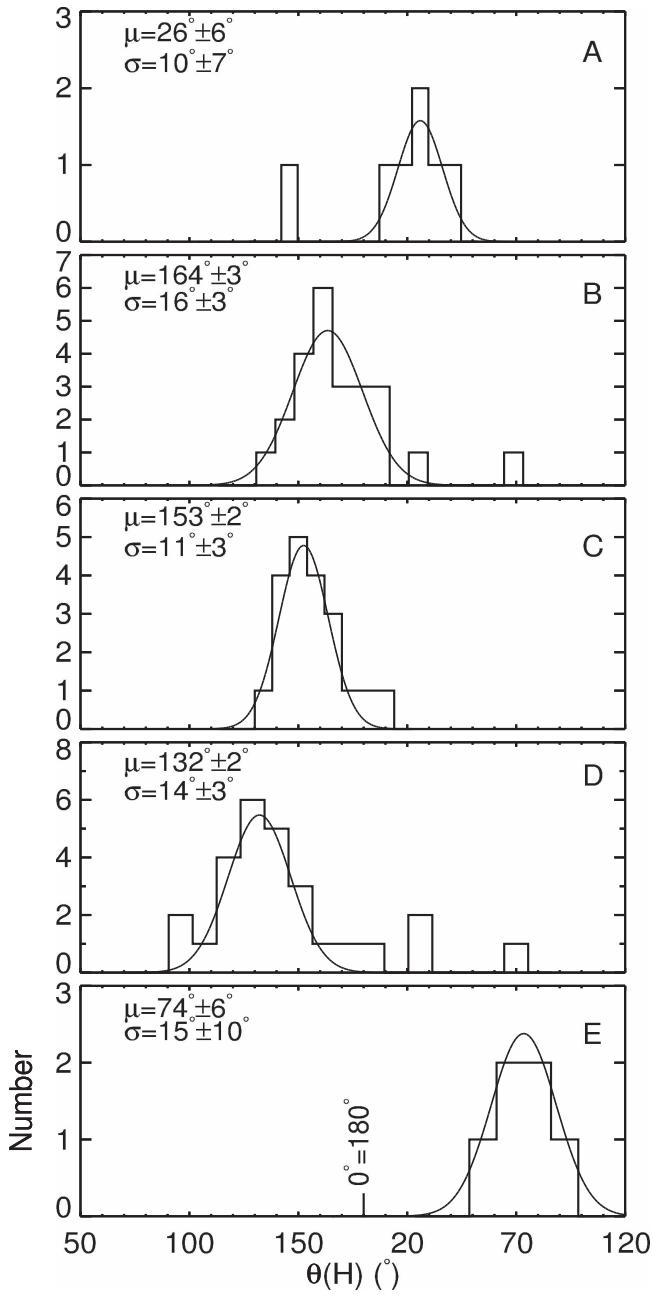
Figure 9. Frequency distribution of $\theta(H)$ for regions A, B, C, D, and E. Gaussian fits are shown with black curves. The mean and uncertainties along with their fit errors are mentioned in each panel.
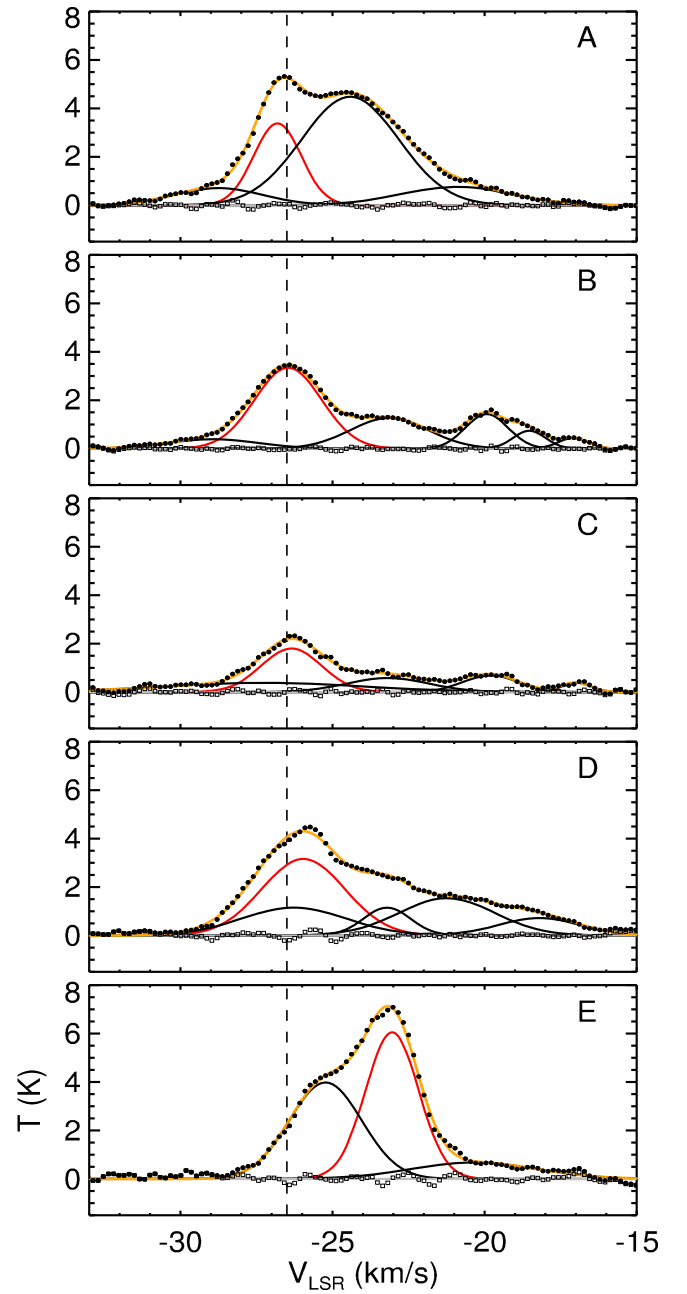

Figure 10. Mean $T(K)$ vs. V_{LSR} (km s^{-1}) spectra for regions A, B, C, D, and E (see Figure 8) from the ^{13}CO$(1-0)$ data of Purcell et al. (2009). Observed data points are shown with filled dots. The spectrum of each region was fit with multiple Gaussians, shown by the black lines. The combined spectrum is shown with a thick orange line. The mean velocity corresponding to the RCW 57A region is drawn at -26.5 km s^{-1} using a dashed line.

the E region, containing a BRC, has a contribution from the expanding I-fronts alone, while the rest of the regions had influences from both expanding I-fronts and outflowing gas. Therefore, the gas velocity dispersion due to the cloud turbulent component (red lines in Figure 10) is well-decomposed from the other components using multi-Gaussian spectrum fitting.

4.3.3. Number Density: $n(H_2)$

Herschel PACS (Poglitsch et al. 2010) 160 μm and SPIRE (Griffin et al. 2010) 250, 350, and 500 μm images of RCW 57A were used to construct a dust column density map using a modified blackbody function (details are given in Appendix D).

The resolution of the final column density map is $36''.4$. To obtain the number densities, we further used Plummer-like profile fitting on the column density profiles to obtain the volume density map as described below.

To construct the column density ($N(H_2)$) profiles, first we manually identify the cloud spine using the pixels that have maximum column densities and are distributed along the filament. Thus, the identified spine, depicted by the green squares in Figure 12(c), divides the entire cloud region into two parts, the NW and SE. Second, for each spine element, we identify the $N(H_2)$ profile elements distributed on a line that

Table 3
Multiple Gaussian Fitted Components of the ^{13}CO Brightness Temperature (T) versus V_{LSR} Spectra of Regions A, B, C, D, and E

No	T_{peak} (K)	V_{LSR} (km s^{-1})	σ (km s^{-1})
		Region A	
1[a]	3.38 ± 0.42	-26.81 ± 0.13	0.78 ± 0.12
2	4.48 ± 0.28	-24.42 ± 0.16	1.60 ± 0.13
3	0.71 ± 0.29	-28.75 ± 0.88	1.45 ± 0.74
4	0.76 ± 0.25	-20.94 ± 0.90	1.81 ± 0.69
		Region B	
1[a]	3.34 ± 0.33	-26.46 ± 0.16	1.10 ± 0.14
2	1.43 ± 0.39	-19.93 ± 0.31	0.70 ± 0.29
3	1.27 ± 0.28	-23.13 ± 0.48	1.28 ± 0.45
4	0.39 ± 0.27	-28.95 ± 1.55	1.51 ± 1.24
5	0.74 ± 0.44	-18.53 ± 0.56	0.53 ± 0.46
6	0.44 ± 0.45	-17.09 ± 0.81	0.49 ± 0.66
		Region C	
1[a]	1.80 ± 0.46	-26.35 ± 0.29	0.99 ± 0.24
2	0.38 ± 0.28	-27.22 ± 2.21	3.27 ± 2.05
3	0.58 ± 0.31	-23.18 ± 1.03	1.35 ± 1.10
4	0.69 ± 0.33	-19.79 ± 0.66	0.91 ± 0.66
5	0.39 ± 0.45	-16.99 ± 0.78	0.48 ± 0.68
		Region D	
1[a]	3.16 ± 1.31	-25.96 ± 0.49	1.37 ± 0.34
2	1.15 ± 1.19	-26.27 ± 1.45	1.72 ± 1.07
3	1.54 ± 0.30	-21.24 ± 0.44	1.57 ± 0.39
4	1.15 ± 0.42	-23.21 ± 0.38	0.77 ± 0.35
5	0.72 ± 0.29	-18.20 ± 0.80	1.34 ± 0.64
		Region E	
1[a]	6.05 ± 0.38	-23.04 ± 0.08	0.87 ± 0.07
2	3.98 ± 0.30	-25.23 ± 0.14	1.19 ± 0.12
3	0.68 ± 0.24	-20.34 ± 1.08	2.05 ± 0.96

Note.
[a] These Gaussian spectra correspond to the cloud velocity and are shown by the thick red lines in Figure 10. The gas velocity dispersion (σ) and error corresponding to the cloud component for each region are also quoted in column 9 of Table 2.

bisects the filament long axis and passes through that spine element. The dimensions of the spine elements as well as the $N(H_2)$ profile elements are chosen to be $36\farcs4 \times 36\farcs4$. To achieve Nyquist sampling, the separation between adjacent elements was chosen as $18\farcs2$. Third, we constructed $N(H_2)$ profiles as a function of projected distances from the filament spine elements toward both the NW and SE regions; they are plotted using gray circles in Figures 12(a) and (b), respectively. Every point and its uncertainty, in these plots correspond to the mean and standard deviation of the column density values in a particular $N(H_2)$ profile element. The mean column density profiles, using distance-wise averaged column densities of the $N(H_2)$ profile elements distributed parallel to the spine, are shown by the red filled circles. Similarly, the error bars correspond to the standard deviations in the corresponding mean column densities of the $N(H_2)$ profile elements.

Assuming that the filament follows an idealized cylindrical model, we extracted the volume density ($n(r)$) profile corresponding to each $N(H_2)$ profile by using the Plummer-like profile (Nutter et al. 2008; Arzoumanian et al. 2011; Juvela et al. 2012; Palmeirim et al. 2013) fit to the $N(H_2)$ profile,

$$n(r) = \frac{n_c}{[1 + (r/R_{flat})^2]^{(p/2)}}, \quad (6)$$

$$N(r) = \frac{A_p n_c R_{flat}}{[1 + (r/R_{flat})^2]^{(p-1)/2}}. \quad (7)$$

The factor $A_p = \pi$ is estimated using the equation $A_p = \int_{-\infty}^{+\infty} [(1 + u^2)^{p/2} \cos i]^{-1} du$ (Arzoumanian et al. 2011) and by assuming that the filament is on the plane of the sky, implying an inclination angle of $i = 0$, and $p = 2$. In Equation (7), $N(r)$ is the column density profile as a function of offset distance (r) from the cloud spine. The fitting was performed using the IDL MPFIT nonlinear least-squares fitting program (Markwardt 2009), and it extracted three parameters: (i) n_c, the central mean volume density of the spine point, (ii) R_{flat}, the radius within which the $N(H_2)$ profile is flat, and (iii) p, the power-law index that determines the slope of the power law falling beyond R_{flat}. The Plummer-like profile fit was performed only to the data spanning to ~ 5 pc (7.3 arcmin) from the spine, beyond which the background column density dominates (horizontal dashed lines in Figures 12(a) and (b)). The fitted values of n_c, R_{flat}, and p are $(7.6 \pm 1.3) \times 10^4$ cm^{-3}, 0.24 ± 0.11 pc, and 2.1 ± 0.1 for the NW part (Figure 12(a)), and $(5.1 \pm 0.9) \times 10^4$ cm^{-3}, 0.37 ± 0.18 pc, and 2.0 ± 0.1 for the SE part (Figure 12(b)). These fit results, as indicated in the plots, are similar.

The volume density map, created using the $n(r)$ profiles of all filament spine elements, is shown in Figure 12(c). Since we considered the spine point on the filament as the zeroth element while performing Plummer-like profile fitting for both the NW and SE regions, each spine point will have two volume density values and are averaged in the final map. The minimum and maximum $n(H_2)$ values on the filament spine lie between 2.48×10^3 cm^{-3} and 1.52×10^5 cm^{-3}. The mean $n(H_2)$ values for pixels at the extreme end of the NW and SE regions are 111 ± 26 cm^{-3} and 228 ± 74 cm^{-3}, respectively. This implies that RCW 57A is still embedded in a diffuse background cloud.

We found that more than 95% of the polarization vectors are centered outside of the blue isodensity contour corresponding to the volume density $n(H_2) = 13,000$ cm^{-3}. It implies that our NIR polarimetry fails to trace adequately the highly extincted parts as shown in Figure 12(c). Therefore, we exclude the pixels with $n \geqslant 13,000$ cm^{-3} while estimating the mean volume densities in regions A, B, C, D, and E. The means and Poisson errors (standard deviation divided by the square root of the number of measurements) of the volume densities for the five regions (A, B, C, D, and E) are estimated and are listed in column 10 of Table 2. More details on producing the volume density map from the column density can also be found in Smith et al. (2014) and Hoq et al. (2017).

It should be noted here that there exist 12 stars within the high column density regions (within the contour of the volume density $n(H_2) = 13,000$ cm^{-3} or column density $N(H_2) \simeq 1 \times 10^{23}$ cm^{-2}). Only one star (star ID = 290; Table 1) is found to lie on the intrinsic locus of the late-type stars in the NIR TCD (with $[J - H] = 0.56 \pm 0.01$ and $[H - K_s] = 0.19 \pm 0.01$). The polarization characteristics ($P(H) = 0.55 \pm 0.13$ and $\theta(H) = 68.5 \pm 6.5$) of this star are consistent with those of the FG stars. Although this star is
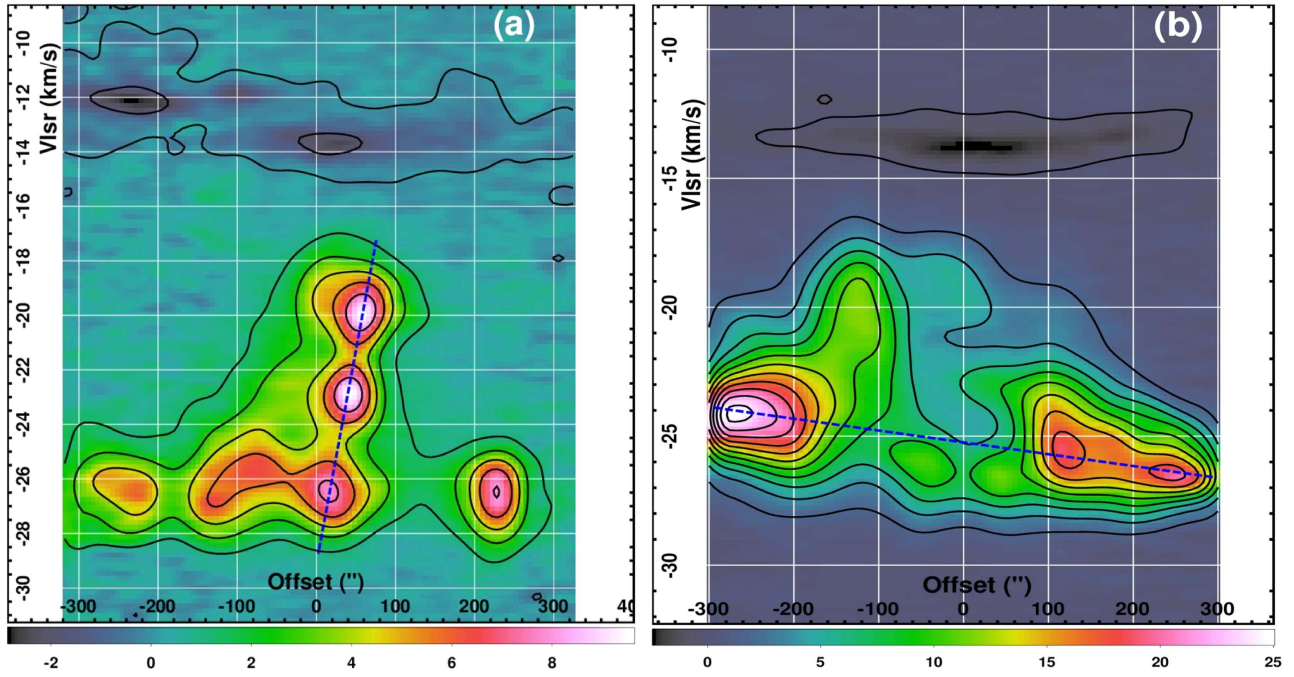
Figure 11. (a) Position−velocity diagram using a cut along the probable orientation of outflowing gas (cut "1" with a position angle = 163°, and central offset coordinates $\alpha = 11^{\rm h}12^{\rm m}06^{\rm s}$, $\delta = -61°18'56''$ [J2000]). Contours are plotted at CO intensities ranging from −3 K to 10 K with a step of 1 K. The blue dotted line connects the three brightest intensity points along the y-axis denoting a velocity gradient of 13 km s^{-1} pc^{-1}. (b) Same as (a) but for a cut along the cloud major axis (cut "2" with a position angle = 65°, and central offset coordinates $\alpha = 11^{\rm h}12^{\rm m}04^{\rm s}$, $\delta = -61°18'44''$ [J2000]). Contours are plotted at CO intensities ranging from −2 to 26 K with a step of 2 K. The blue dotted line connects the brightest intensity points along the x-axis denoting a velocity gradient of 0.35 km s^{-1} pc^{-1}. The unit of the color scale in both panels is K.

classified as a BG star based on its $[H - K_s] > 0.15$, this star could be located close, but foreground, to the cloud. The remaining 11 stars are consistent with either reddened cluster members embedded in the cloud or reddened field stars lying in the outskirts of the cloud but projected on the high-density parts of the cloud region.

4.4. Magnetic Field Strength Using the Chandrasekhar–Fermi Method

Using the dispersion in the polarization angles ($\sigma_{\theta(H)}$; column 8 of Table 2), velocity dispersion values ($\sigma_{V_{\rm LSR}}$; column 9 of Table 2), and mean volume densities ($n({\rm H_2})$; column 10 of Table 2) for the five regions of RCW 57A, we estimated the B-field strength using the Chandrasekhar & Fermi (1953) relation,

$$B = Q\ \sqrt{4\pi\rho}\left(\frac{\sigma_{V_{\rm LSR}}}{\sigma_{\theta_{\rm H}}}\right). \qquad (8)$$

The mass density $\rho = n({\rm H_2})m_H\mu_{{\rm H_2}}$, where $n({\rm H_2})$ is the hydrogen volume density, $m_{\rm H}$ is the mass of the hydrogen atom, and $\mu_{{\rm H_2}} \approx 2.8$ is the mean molecular weight per hydrogen molecule and includes the contribution from helium. The correction factor $Q = 0.5$ is included based on the studies using synthetic polarization maps generated from numerically simulated clouds (Heitsch et al. 2001; Ostriker et al. 2001), which suggest that for $\sigma_\theta \leqslant 25°$, the B-field strength is uncertain by a factor of two. Uncertainties in the B-field strength were estimated by propagating the errors in $\sigma_{\theta(H)}$, $\sigma_{V_{\rm LSR}}$, and $n({\rm H_2})$ values. The estimated B-field strengths and corresponding uncertainties are given in column 11 of Table 2. The uncertainties in the B-fields, derived by

propagating errors in $n({\rm H_2})$, $\sigma_{V_{\rm LSR}}$, and $\sigma_{\theta_{\rm H}}$, are considerably large (see column 11 of Table 2). We also estimate the B-field strengths and corresponding uncertainties without considering errors in the $\sigma_{\theta_{\rm H}}$ values. The resultant B-field strengths, given in column 12 of Table 2, for regions A, B, C, D, and E are $123 \pm 21\,\mu{\rm G}$, $89 \pm 13\,\mu{\rm G}$, $63 \pm 15\,\mu{\rm G}$, $108 \pm 27\,\mu{\rm G}$, and $74 \pm 8\,\mu{\rm G}$, respectively. The mean B-field strength over the five regions is estimated to be $91 \pm 8\,\mu{\rm G}$.

To understand the importance of B-fields with respect to turbulence, we estimated the magnetic pressure and turbulent pressure using the relations $P_B = B^2/8\pi$ and $P_{\rm turb} = \rho\sigma_{\rm turb}^2$ (where $\sigma_{\rm turb} = \sigma_{V_{\rm LSR}}$ is given in Table 2), respectively, and the results are given in Table 4. The mean $P_B/P_{\rm turb}$ is estimated to be 2.4 ± 0.6. These estimated parameters suggest that the magnetic pressure is more than the turbulent pressure at least by a factor of ∼2 in all five regions, signifying the dominant role of B-fields over turbulence. For the five regions together, the mean magnetic and turbulent pressures are estimated to be $(35 \pm 7) \times 10^{-11}$ (dyn cm^{-2}) and $(15 \pm 3) \times 10^{-11}$ (dyn cm^{-2}), respectively. Danziger (1974) estimated the mean electron density, n_e, to be ∼20 cm^{-3}, and mean electron temperature, T_e, to be ∼10,000 K for the RCW 57A region. For the entire region, the thermal pressure $P_{\rm th}$ using the relation $P_{\rm th} \simeq 2n_e kT_e$ (where k is the Boltzmann constant) is estimated to be 6×10^{-11} dyn cm^{-2}, which is smaller than the mean magnetic pressure. The ratio of the mean magnetic to thermal pressure, $P_B/P_{\rm th}$, is found to be ∼6. A lower value of $P_{\rm th}$ again suggests dominant magnetic pressure over thermal pressure. Therefore, in comparison to thermal and turbulent pressures, magnetic pressure plays a crucial role in guiding the expanding I-fronts or outflowing gas in RCW 57A. The implications on the relative importance of B-field pressure in comparison to
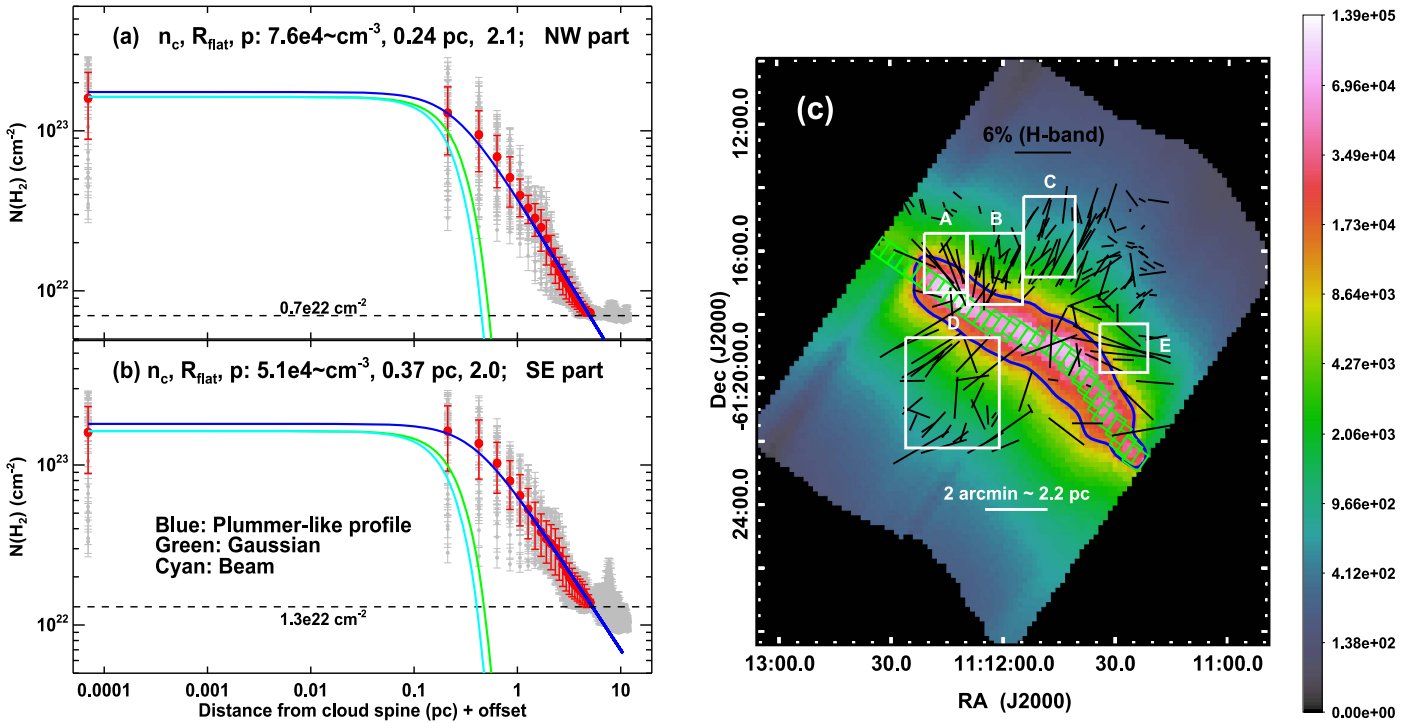
Figure 12. (a) Plummer-like profile fitting (blue line) of the mean column density profile (red points) of the NW region of RCW 57A. Gray points corresponds to the individual NW column density profiles. Cyan and green lines correspond to the beam size (FWHM = $36\rlap{.}''4$ = 0.42 pc) of the volume density map and Gaussian fit (FWHM = 0.50 ± 0.18 pc), respectively. (b) Same as (a) but for the SE region of RCW 57A. In both panels (a) and (b), the results from the Plummer-like profile fitting are mentioned. Dashed horizontal lines represent the background column densities in the NE and SW regions. (c) The volume density map constructed using the Plummer-like profile fitting of the column density map. Spine points are shown by green squares with dimension of $36\rlap{.}''4 \times 36\rlap{.}''4$, which are separated by $18\rlap{.}''2$. The units of the color scale is cm^{-3}. The thick blue contour corresponds to the volume density $n = 13{,}000\ cm^{-3}$. The black vectors and white boxes are the same as those in Figure 8. A reference length scale with $2'$ corresponding to 2.2 pc is shown.

Table 4
Magnetic and Turbulent Pressures along with Their Uncertainties in Regions A, B, C, D, and E

Region (1)	P_B 10^{-11} (dyn cm^{-2}) (2)	P_{turb} 10^{-11} (dyn cm^{-2}) (3)	P_B/P_{turb} (4)
A	60 ± 20	15 ± 5	4 ± 2
B	32 ± 9	20 ± 6	2 ± 1
C	16 ± 8	5 ± 2	3 ± 2
D	46 ± 23	22 ± 11	2 ± 1
E	22 ± 5	11 ± 3	2 ± 1

Note. In this table, the B-field pressure values and their uncertainties are derived using the B-field strength and corresponding uncertainties given in column 12 of Table 2.

turbulent and thermal pressures on the formation and evolution of bipolar bubble is discussed in the Section 5.3.

5. Discussion

5.1. Anisotropic Distribution of Material in the Cloud and the Bipolar Bubble

Based on the CO and *Spitzer* images, number of stars with polarization detection, and the column density profiles we infer for the distribution of gas and dust in RCW 57A. The quiescent molecular cloud gas traced by CO (red background in Figure 7) is absent at the footpoints of, as well as along, the bipolar bubbles. Moreover, the spatial distributions of the CO gas and the bubbles (green background in the *Spitzer* images) appear to

be anti-coincident with each other. This implies that cloud material has either been eroded or blown out by the expanding I-fronts, outflowing gas, or strong stellar winds from the embedded early-type protostars. Therefore, the CO and *Spitzer* maps suggest that the bipolar bubble likely blown by the massive stars emanated stellar winds, outflowing gas, and expanding I-fronts (see Townsley 2009).

Although the SE bubble appears to be closed toward the SE, the NW bubble is widely extended toward the NW (Figures 1 and 7) and exhibits large-scale loops, likely due to the anisotropic distribution of material toward the SE and NW regions. This is further corroborated by the following facts. Although the area covered together by regions A, B, and C (located in the NW) is similar to that covered by D (located in SE), the total number of background stars with polarization detection (51) in A, B, and C exceeds that in D (21; see Table 2 and Figures 7 and 8). Furthermore, the mean $N(H_2)$ profiles suggest that the anisotropic distribution of gas and dust in RCW 57A i.e., the SE part ($N(H_2) \sim 1.3 \times 10^{22}\ cm^{-2}$), has relatively more background material than in the NW ($N(H_2) \sim 0.70 \times 10^{22}\ cm^{-2}$) as depicted by the dashed lines in Figures 12(a) and (b). A similar asymmetric distribution of column density profiles was seen toward other regions (e.g., the Taurus B211/3 filament; Palmeirim et al. 2013).

An X-ray study (Townsley et al. 2011, see their Figures 3 and 4) revealed the presence of an OB stellar association (NGC 3576OB) toward the NW of the main embedded star-forming region RCW 57A (or NGC 3576 GHIIR). Furthermore, the presence of hard X-ray emission and a pulsar (+PSR

J1112–6103 and PWN) in the NGC 3576OB region suggests the fast occurrence of supernova events. This supernova, together with the OB stars of the NGC 3576OB stellar association, most probably evacuated the material in the NW part of RCW 57A. This could be the plausible reason behind the low-density material observed in the NW region. The observed large-scale loops in the NE possibly formed due to the newly formed material as a result of the expanding I-fronts driven by the embedded massive protostars of RCW 57A.

A high-velocity outflow signature is discernible close to eastward from the center, while the same feature is absent westward as shown in Figure 11(b). This could be attributed to the confined ionized gas flow toward the west from the center, possibly due to the presence of a dense clump (thin black contours in Figure 7). The high-velocity component is only seen toward the east, which implies a dearth of dense material there, and hence, the ionized gas expanded with relatively more velocity. de Pree et al. (1999) and Purcell et al. (2009) have also shown that the H II region expands more freely toward the east and is bounded on the west.

5.2. Column Density Profiles: Filament Width and B-field Support

We fitted a Gaussian to the mean column density profiles spread over ∼5 pc radii, and the resultant FWHM, corresponding to the filament characteristic width, is found to be 1.55 ± 0.09 pc. However, a constant filament width of ∼0.1 pc was determined for the central dense sections of the filaments of nearby star-forming regions in the *Herschel* Gould Belt survey by fitting a Gaussian to the inner sections (radii up to 0.3–0.4 pc) of the filaments (Arzoumanian et al. 2011). Therefore, we fit a Gaussian to the inner 1 pc width of the clubbed mean column density profiles of the NW and SE regions, and the resultant σ and FWHM are found to be 0.21 ± 0.08 pc and 0.50 ± 0.18 pc, respectively. Within the error, the filament width (0.50 pc; green lines in Figures 12(a) and (b)) of RCW 57A is higher than the constant filament width of ∼0.1 pc (Arzoumanian et al. 2011). Filament widths larger than 0.1 pc (spanning over 0.1–1 pc with typical widths of ∼0.2–0.3 pc) have also been witnessed in a number of studies (e.g., Hennemann et al. 2012; Juvela et al. 2012). However, the filament width of RCW 57A has not been resolved because of the limited resolution ($36\overset{''}{.}4$ corresponds to 0.42 pc as shown by the cyan lines) of the column density map.

The mean power-law index $p = 2.02 \pm 0.05$, derived from the Plummer-like profile fitting for RCW 57A, is consistent with other studies (Arzoumanian et al. 2011; Juvela et al. 2012; Palmeirim et al. 2013; Hoq et al. 2017). A similar value of this index ($p = 2$) is expected if the filament is supported by B-fields (Hennebelle 2003; Tilley & Pudritz 2003), in accordance with our observational results supporting the active role of B-fields in the formation and evolution of filaments, as described in Section 5.3 below.

5.3. Evolutionary Scenario of the Filament and Bipolar Bubble

Based on the morphological correlations among the (i) dense filamentary cloud structure seen in the submillimeter (in the 0.87 mm ATLASGAL and 1.1 mm SIMBA dust continuum emission maps), (ii) bipolar bubble seen in mid-infrared images, and (iii) B-field morphology of RCW 57A traced by NIR polarimetry, we postulate a scenario illustrated by the four schemas in Figure 13. Each schema describes our observational evidence along with our prediction at a particular evolutionary state of RCW 57A.

Schemas A and B: Per the background star polarimetry, the filament (position angle ∼60°; Figure 7) is oriented perpendicular to the B-fields (the dominant component of θ $(H) = \sim163°$; Figure 6(d)). From this observational evidence, we speculate the formation history of the filament and the role of the B-fields in them. Initially, a subcritical molecular cloud is supported by the B-fields, as shown in schema A; it is later compressed into a filamentary molecular cloud due to B-field-guided gravitational contraction as per schema B.

Although the role of B-fields in the formation and evolution of filamentary molecular clouds is still a matter of debate, their morphology with respect to the geometry of filaments is well established. The geometry of B-fields in a molecular cloud is mainly governed by the relative dynamical importance of magnetic forces to gravity and turbulence.

If the B-fields are dynamically unimportant compared to the turbulence, then random motions dominate the structural dynamics of the clouds, and the field lines would be dragged along the turbulent eddies (Ballesteros-Paredes et al. 1999). In that case, B-fields would exhibit chaotic or disturbed B-field structures. Based on the fact that the B-field structure is more regular with an hourglass morphology and that B-field pressure dominates over turbulent pressure (see Section 4.4), we do not favor a weak B-field scenario in RCW 57A.

If B-fields are dynamically important, then the support against gravity in the molecular cloud is rendered predominantly by the B-fields. In this case, B-fields would be aligned, preferentially, perpendicular to the major axis of the cloud (Mouschovias 1978). This is expected as the cloud tends to contract more in the direction parallel to the B-fields than in the direction perpendicular to it. Recent polarization studies have also demonstrated that B-fields are well-ordered near dense filaments and are perpendicular to their long axis (Moneti et al. 1984; Pereyra & Magalhães 2004; Alves et al. 2008; Chapman et al. 2011; Sugitani et al. 2011; Li et al. 2013; Palmeirim et al. 2013; Franco & Alves 2015; Cox et al. 2016; Planck Collaboration et al. 2016a). Numerical simulations have also shown that filamentary molecular clouds form by gravitational compression guided by B-fields (e.g., Nakamura & Li 2008; Li et al. 2013). Therefore, we believe that the filament in RCW 57A could have formed due to the gravitational compression of cloud along the B-fields.

Schema C: Due to the accumulation of more mass at the center, the filament reaches a supercritical state from its initial B-field-supported subcritical state. B-fields are dragged along the gravity-driven material contraction toward the strong gravitational potential at the cloud center, and subsequently they are configured into an hourglass morphology (schema C). Similar hourglass morphologies of B-fields were observed toward the Orion molecular cloud 1 (Schleuning 1998; Vaillancourt et al. 2008; Ward-Thompson et al. 2017) and Serpens cloud core (Sugitani et al. 2010), signifying ongoing gravitational collapse.

In RCW 57A, B-fields in some portions exhibit clear evidence for hourglass morphology. In the NE part of the filament (covered by two regions, A and D; see Figure 8), B-fields are bent by ∼90° as the mean $\theta(H)$ for region A is
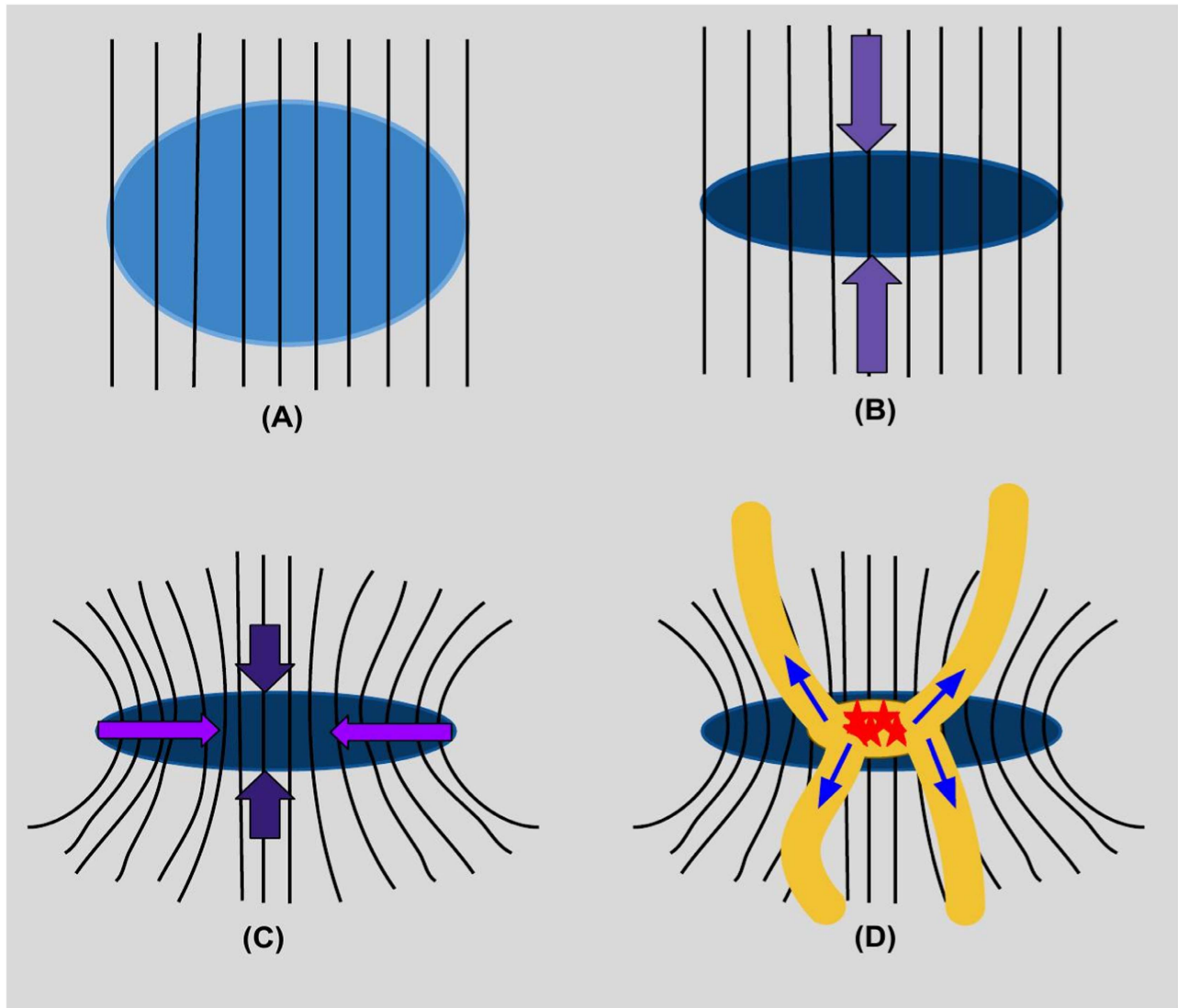
Figure 13. Schematic diagram illustrating the possible connection among the filament, bipolar bubble and *B*-fields. Initially, a subcritical molecular cloud permeated by uniform *B*-fields (schema A) could have gravitationally compressed along the *B*-fields into a filament (schema B). Later, as mass accumulated at the center of the filament, a gravitationally contracting cloud could have pulled the *B*-fields along the cloud material toward the central region. Thus, the *B*-fields followed a clear hourglass morphology when the collapsing cloud reached a supercritical state (schema C). The dense and highly pressurized H II region formed due to the formation of massive stars at the cloud center (schema D). Further, the propagation of I-fronts and stellar winds is rather controlled by the an isotropic distribution of gas and dust in the filament. The presence of *B*-fields in an hourglass morphology further introduced an additional anistropic pressure in favor of expanding I-fronts or outflowing gas so as to form the bipolar bubble (schema D).

$\sim 26°$ and $\sim 132°$ for region D (see column 7 of Table 2). Therefore, *B*-fields are distorted in the NE part of the filament, signifying a collapsing filamentary molecular cloud. However, this similar distortion is not clearly apparent in the SW part of the filament, partly because the light from the background stars is obscured by the dense cloud material. Therefore, the NIR polarimetric observations were unable to detect sufficient numbers of background stars in the SW part to delineate the detailed structure of the *B*-field there.

Schema D: Gravitational instability caused the filament fragmentation into seven cores (blue diamonds in Figure 7), evident from the dust continuum emission maps (André et al. 2008) as well as dense gas tracers (Purcell et al. 2009). Star formation began at the central region due to the onset of gravitational collapse, during which *B*-fields were not strong

enough to stop the cloud collapse. Ionization and shock fronts, driven by the H II region, are propagated in to the ambient medium. Interaction between the H II region and dense cloud material is evident from Figure 7, and as a consequence of this, several IRSs are formed at the boundary of the interaction, signifying triggered star formation at the edges of the H II region of RCW 57A.

Our observational results suggest that *B*-field pressure dominates over thermal pressure (see Section 4.4), implying an active role of *B*-fields in governing the feedback processes. Since *B*-fields are observed to be responsible for the formation of the filament in RCW 57A (Schema B), it is expected that *B*-fields anchored through the filament may also have a significant influence on the expanding I-fronts. In addition to the anisotropic pressure that the I-fronts experience while

they expand anisotropically in the filament, they undergo an additional anisotropic pressure in the presence of strong B-fields (Bisnovatyi-Kogan & Silich 1995). As a result, I-fronts experience accelerated flows along the B-fields (i.e., low pressure) and hindered flows (i.e., high pressure) in the direction perpendicular to the B-fields (Tomisaka 1992; Gaensler 1998; Pavel & Clemens 2012; van Marle et al. 2015). Therefore, I-fronts expand a greater extent along the hourglass shaped B-fields, and eventually form the bipolar bubble as shown in schema D of Figure 13.

Similar applications for the influence of B-fields on I-fronts have been found in other environments. Bubbles around young H II regions and supernova remnants have been found to be elongated along the Galactic B-field orientation (Tomisaka 1992; Gaensler 1998; Pavel & Clemens 2012). Falceta-Gonçalves & Monteiro (2014) showed that strong B-fields can lead to the formation of a bipolar planetary nebula. van Marle et al. (2015) investigated the influence of B-fields on the expanding circumstellar bubble around a massive star using magnetohydrodynamical simulations. They found that that the weak B-fields cause circumstellar bubbles to become an ovoid, rather than a spherical, shape. On the other hand, strong B-fields lead to the formation of a tube-like bubble.

Therefore, according to the proposed evolutionary scenario (Figure 13), initially, B-fields in molecular clouds may be important in guiding the gravitational compression of cloud material to form a filament. In the later stage, hourglass B-fields might have guided the expansion and propagation of I-fronts to form the bipolar bubble.

5.4. B-fields Favoring the Formation of a Massive Cluster at the Center of the Filament

Based on the presence of 29 NIR-excess sources (Persi et al. 1994) and the finding of 51 stars earlier than A0 (Maercker et al. 2006), it was found that RCW 57A hosts a massive infrared cluster at the center (within the cyan contour enclosing the H II region in Figure 7) of the filament. Furthermore, the *Chandra* X-ray survey by Townsley et al. (2014; see also Townsley et al. 2011) provided the first detailed census of the members in the embedded massive young stellar cluster (MYSC; see their Figures 9(c) and (d)). Their study unraveled many highly obscured but luminous X-ray sources (one source exhibits photon pile-up) that are likely the cluster's massive stars ionizing its H II region. This highly obscured X-ray cluster is situated at the SW edge of the infrared cluster. The formation history of this cluster is poorly understood. Below, we propose that the large-scale B-fields traced by NIR polarimetry may also govern their crucial role in the formation of this massive cluster.

Initial turbulence in the molecular clouds may decay rapidly. To maintain turbulence in the cloud and hence to maintain cloud stability against rapid gravitational collapse, supersonic turbulence should be replenished by means of protostellar outflows. In the model of outflow-driven turbulence cluster formation (Li & Nakamura 2006; Nakamura & Li 2007, 2011, and references therein), B-fields are dynamically important in governing two processes. First, the outflow energy and momentum are allowed by the B-fields to escape from the central star-forming region into the ambient cloud medium. Second, B-fields guide the gravitational infalling material (just outside of the outflow zone) toward the central region.

Therefore, the competition between protostellar outflow-driven turbulence and gravitational infall regulates the formation of stellar clusters in the presence of dynamically important B-fields. Observational signatures toward the Serpens cloud core (Sugitani et al. 2010) are in accordance with the scenario of a B-field regulated cluster formation: (a) B-fields should align with the short axis of the filament, outflows, and gravitational infall motions, and (b) outflow-injected energy should be more than the dissipated turbulence energy in order to maintain the supersonic turbulence in the cloud. In the case of RCW 57A, the presence of a deeply embedded cluster and the alignment of the I-fronts, outflowing gas, and bipolar bubbles with the NIR-traced B-fields trace the preexisting conditions favoring protostellar outflow-driven turbulence cluster formation in the presence of dynamically strong B-fields.

6. Summary and Conclusions

Though there exist a few studies regarding the formation of bipolar bubbles, none of them has explored the importance of B-fields. Our aim was to understand the morphological correlations among the B-fields, filament, and bipolar bubbles, and their implications for the star formation history in RCW 57A. We conducted NIR polarimetric observations in the JHK_s bands using SIRPOL to delineate the B-field structure in RCW 57A. We employed various means (NIR and MIR color–color diagrams, polarization efficiency diagrams, and polarization characteristics) to exclude YSOs with possible intrinsic polarization. Through our analyses, we separated 97 confirmed foreground stars from the 178 confirmed background stars having H-band polarimetry. Below we summarize the results of our present work.

1. Foreground dust is dominated by a single-component B-field having a mean $\theta(H) \sim 65°$, which is different from the position angle ($101°$) corresponding to the Galactic plane.

2. The polarization values of BG stars are consistent with the dichroic origin of dust polarization and exhibit relatively higher polarization efficiencies, suggesting efficiently aligned dust grains in RCW 57A.

3. The polarization angles of the reddened background stars reveal that the B-field in RCW 57A is configured into an hourglass morphology, which follows closely the structure of the bipolar bubbles. The dominant component of the B-field ($\theta(H) \sim 163°$) is perpendicular to the filament major axis. The orientations of both outflowing gas from the embedded protostars and the expanding I-fronts from the H II region are aligned with the B-fields.

4. The B-field strength averaged over five regions across RCW 57A using the CF method is $91 \pm 8 \, \mu G$. The B-field pressure is estimated to be more than the turbulent and thermal pressures.

5. Morphological correlations among B-fields, filament, and bipolar bubbles, as well as the dominance of B-field pressure over turbulent and thermal pressures, suggest a scenario in which B-fields not only play an important role in the formation of the filamentary molecular cloud but also in guiding the expansion and propagation of I-fronts and/or outflowing gas to form bipolar bubbles. In this picture, B-fields impart additional anisotropic pressure to

expanding I-fronts, from H II regions, expanding and propagating them to greater extent.

6. Protostellar outflow-driven turbulence and gravity in the presence of dynamically important B-fields might be responsible for the cluster formation. Therefore, our study, based on the link among B-fields, filament, and bipolar bubble, traces the preexisting conditions where B-fields might also be important in the formation of the massive cluster in RCW 57A.

Appendix A
Calibration of IRSF Photometry Into 2MASS

The 401 stars having both IRSF and 2MASS data were used to calibrate the IRSF photometry of 702 stars into the 2MASS system using the following relations:

$$J_{2MASS} = J_{IRSF} + \alpha_1 \times [J-H]_{IRSF} + \beta_1, \tag{9}$$

$$H_{2MASS} = H_{IRSF} + \alpha_2 \times [H-K_s]_{IRSF} + \beta_2, \tag{10}$$

$$K_{s\ 2MASS} = K_{s\ IRSF} + \alpha_3 \times [J-K_s]_{IRSF} + \beta_3, \tag{11}$$

$$[J-H]_{2MASS} = \alpha_4 \times [J-H]_{IRSF} + \beta_4, \tag{12}$$

$$[H-K_s]_{2MASS} = \alpha_5 \times [H-K_s]_{IRSF} + \beta_5. \tag{13}$$

Figure 14 depicts the weighted least-squares fittings for magnitudes and colors between IRSF and 2MASS. The fitted coefficients are found to be $\alpha_1 = 0.0462 \pm 0.0033$, $\beta_1 = -2.3812 \pm 0.0040$; $\alpha_2 = -0.0384 \pm 0.0053$, $\beta_2 = -2.1506 \pm 0.0028$; $\alpha_3 = -0.0095 \pm 0.0018$, $\beta_3 = -2.9199 \pm 0.0021$; $\alpha_4 = 1.0719 \pm 0.0051$, $\beta_4 = -0.2696 \pm 0.0060$; and $\alpha_5 = 0.9872 \pm 0.0078$, $\beta_5 = 0.7828 \pm 0.0042$. These coefficients were used, finally, to transform the instrumental magnitudes and colors of the IRSF system to the 2MASS system.

Appendix B
B-field Structure Around a BRC

The H-band polarimetry of 26 background stars covering the BRC depicts compressed B-fields along the rim of the BRC as
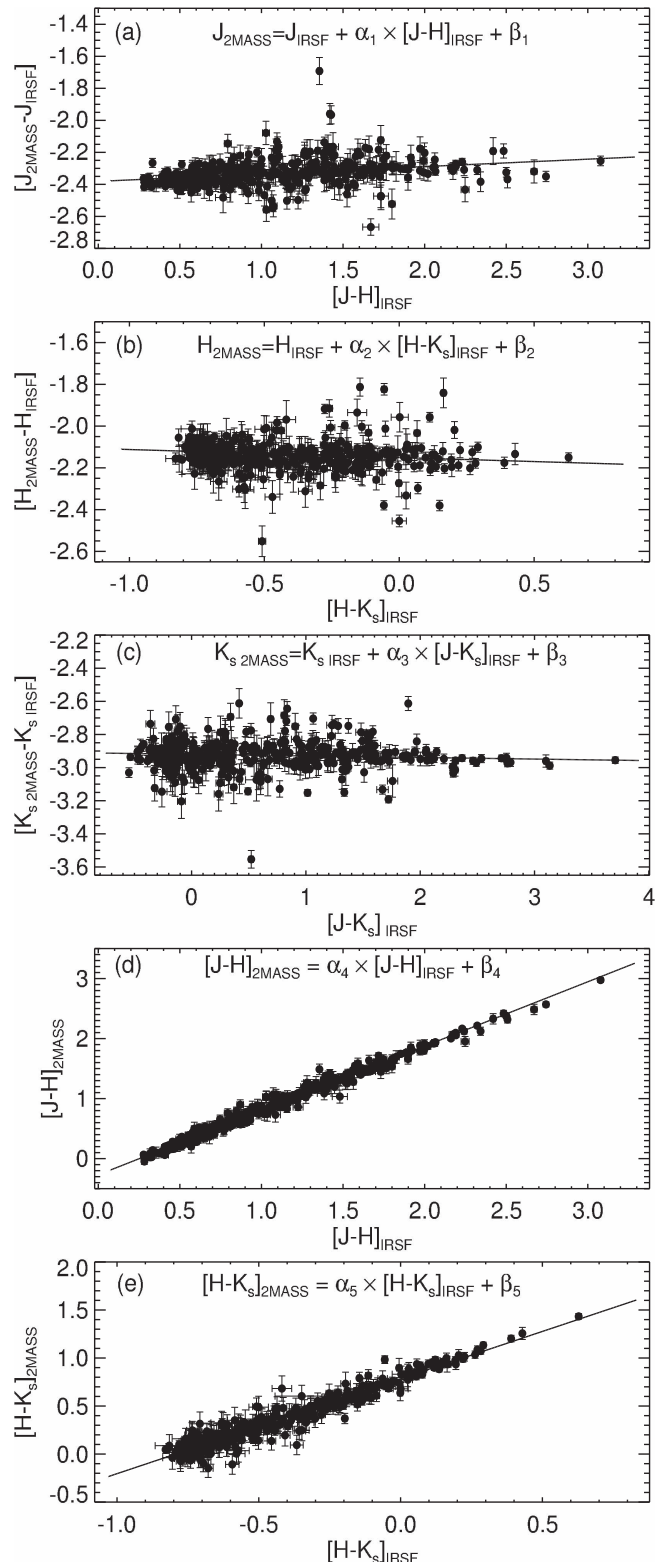

Figure 14. Calibration between IRSF and 2MASS systems by using the JHK_s photometric magnitudes of 401 stars whose photometric uncertainties are less than 0.1 mag. (a) $[J-H]_{IRSF}$ vs. $[J_{2MASS} - J_{IRSF}]$ (b) $[H-K_s]_{IRSF}$ vs. $[H_{2MASS} - H_{IRSF}]$, (c) $[J-K_s]_{IRSF}$ vs. $[K_{s\ 2MASS} - K_{s\ IRSF}]$ (d) $[J-H]_{IRSF}$ vs. $[J-H]_{2MASS}$, and (e) $[H-K_s]_{IRSF}$ vs. $[H-K_s]_{2MASS}$.

shown in Figure 15. BRCs are formed in and around H II regions due to the interaction of I-fronts with the ambient medium. It is unclear whether the preexisting inhomogeneities

in the medium (in the form of globules) or instability in the expanding I-fronts is important in the formation of these structures (Kahn 1958; Williams et al. 2001), but both might be acting albeit on different length scales (Mackey & Lim 2013). Though thermal pressure enhanced by the ionizing radiation governs the entire formation process of BRCs, it has been shown that B-field pressure and its orientation may also play a key role in shaping the density distribution of the BRCs as well as their structure (Motoyama et al. 2013). Motoyama et al. (2013) also stated that the evolution of the BRCs depends on the orientation of the B-fields with respect to the direction of the exciting source(s) (or I-front).

Mackey & Lim (2011a, 2011b, 2013) and Mackey (2012) performed 3D radiation-magnetohydrodynamic (RMHD) simulations of the photoionization of dense clouds threaded by B-fields with different orientations and strengths with respect to the direction of the ionizing source. Here we correlate our results, especially with those models involving different B-field strengths but oriented perpendicular to the direction of the propagating I-fronts. The B-fields in the models involving weak ($\sim$15 μG) and moderate ($\sim$50 μG) strengths are swept into alignment with the pillar/globule during the later evolutionary stages (Mackey & Lim 2011a; see also Henney et al. 2009), whereas at the head of the cometary globule, B-fields are compressed into a curved morphology by closely following the bright rim of the cometary globule (see the R5 model at the top and middle panels of Figures 2 and 3 of Mackey & Lim 2011a), similar to our present observations toward the BRC (Figure 15). While weak B-field models result in B-fields more significantly aligned parallel to the pillars, strong B-field models ($\sim$160 μG) produce ionized gas confined to a dense ribbon which stands apart from the globule and shields the globule from the ionizing radiation. In the strong B-field model, B-fields do not exhibit an obvious change in their orientation both at the head or tail of the pillar (see the R8 model results at the bottom panels of Figures 2 and 3 of Mackey & Lim 2011a).

The B-field strength for the region E associated with the BRC (see Figures 7 and 8) is estimated to be 74 ± 8 μG. The approximate distance to the BRC from the H II region is $\sim$2.2 pc. B-field orientation in a globule prior to the formation of the BRC would be $\sim$163° (which corresponds to the dominant component of B-fields in the cloud before the onset of star formation; see Figure 6(d) and Section 4.1) and is shown with a dashed cyan line in Figure 15. The direction of propagating ionizing radiation from the H II region with respect to the BRC makes a position angle of 95°, as shown with a green arrow. This implies that the initial B-fields around the BRC ($\sim$163°) are oriented nearly orthogonal to the direction ($\sim$95°) of the I-fronts. Thus, the estimated B-field strength (74 ± 8 μG) and its initial orientation around the BRC are similar to those of the R5 models of Mackey & Lim (2011a) involving perpendicularly oriented B-fields with moderate strength (50 μG). We believe that this BRC might be formed due to a portion of ionizing radiation that is leaked through the low-density parts of the molecular cloud; otherwise, it would have evaporated if all of the radiation from the H II region impinges on the BRC. Therefore, this BRC might experience the influence of thermal pressure equivalent to that emanating from a single O-type star. Mackey & Lim (2011a) also only used a single O-type star as the ionizing source in their models.

According Mackey & Lim (2013), at 400 kyr, for models with moderate B-fields ($\sim$50 μG), vertical motions along the B-fields are initiated (see the left panel of Figure 1 of Mackey & Lim 2013). Due to this, gas flows in response to photoevaporation flows along the B-fields result in the formation of a dense ridge filament elongated parallel to the B-fields. At 500 kyr, a clear cometary globule is formed in which B-fields are aligned with their bright rim, similar to our results. Thus, our results are in accordance with the RMHD models of Mackey & Lim (2011a, 2013) with moderate B-field strength (initially oriented perpendicular to the direction of the radiation propagation). Observational evidence similar to our present results include compressed B-fields along, but behind, the bright rim SFO 74 (Kusune et al. 2015).

Appendix C
Multi-Gaussian Fitting on T versus V_{LSR} Spectra

Initial guess values were provided by a visual inspection of observed spectra. The number of Gaussian components is determined based on the number of peaks appearing in each spectrum. Since "gatorplot.pro" does not provide the errors in the fitted multi-Gaussians, we further used an output of "gatorplot.pro" as an input to the "mpfitpeak.pro" of the Markwardt IDL suite of functions (Markwardt 2009) to ascertain the uncertainties of the fitted measurements. Instead of varying all three parameters of one Gaussian (peak:T_{peak}, center: V_{LSR} and width: $\sigma_{V_{\mathrm{LSR}}}$), we fixed two of them and varied one (similarly, in the case of three Gaussians, out of nine parameters, three were varied and six were kept constant). Likewise, we constrained all the multi-Gaussian components of each spectrum along with their fitted errors using the reduced chi-square minimization method. Equal weights are given to all points of an observed spectrum while fitting was performed.

Appendix D
Column Density Map Using *Herschel* Data

A column density map was constructed using the following relation (Kauffmann et al. 2008)

$$S_\nu^{\mathrm{beam}} = \left(\frac{N_{\mathrm{H_2}}}{2.02 \times 10^{20} \ \mathrm{cm}^{-2}} \right) \times \left(\frac{K_\nu}{0.01 \ \mathrm{cm}^2 g^{-1}} \right)$$
$$\times \left(\frac{\theta_{\mathrm{HPBW}}}{10 \ \mathrm{arcsec}} \right)^2 \times \left(\frac{\lambda}{\mathrm{mm}} \right)^{-3}$$
$$\times \left(\exp\left(1.439 \left(\frac{\lambda}{\mathrm{mm}} \right)^{-1} \left(\frac{T}{10 \ \mathrm{K}} \right)^{-1} \right) - 1 \right)^{-1}, \quad (14)$$

where S_ν^{beam} is the flux per beam (mJy beam^{-1}), $N_{\mathrm{H_2}}$ is the column density, and $K_\nu (=0.1\left(\frac{\nu(\mathrm{GHz})}{1000}\right)^\beta$; ν is the frequency and β is the dust opacity exponent, and is considered to be 2; Arzoumanian et al. (2011), Anderson et al. (2012)) is the dust opacity or specific absorption constant. θ_{HPBW} (arcsec) is the beam width (or half-power bandwidth in arcsec) of the PACS 160 μm (11″.4) and SPIRE 250 μm (18″.1), 350 μm (24″.9), and 500 μm (36″.4) images. λ (mm) is the wavelength and T (K) is the dust temperature. The pixel unit of the PACS 160 μm image is Jy pixel^{-1} and that of SPIRE (250, 350 and
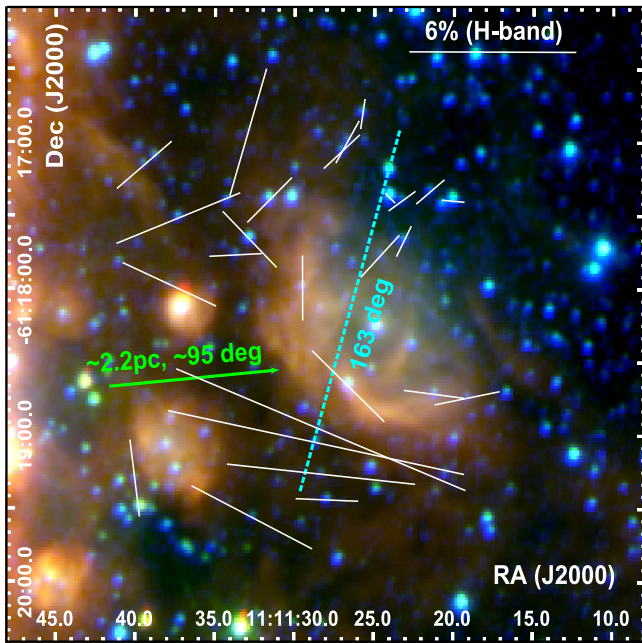
Figure 15. Polarization vectors (white) depicting the *B*-field orientation, using the *H*-band polarimetry of 26 confirmed BG stars, around a BRC located within the white box in Figure 7. Background is the tricolor image ($\sim4.5' \times 4.3'$) made using *Spitzer* IRAC Ch4 (red), IRAC Ch2+Ch3 (green), and 2MASS K_s-band (blue) images. The green arrow with an orientation of $\sim95°$ indicates the direction of the I-front that emanated from the H II region. The dashed cyan line denotes the *B*-field orientation ($\sim163°$) in the star-forming region prior to the formation of the BRC. The reference vector with 6% is shown.

500 μm) is MJy sr^{-1}. The final pixel units were converted into mJy beam^{-1}using the following relations[16]:

$$M\left(\frac{\text{Jy}}{\text{sr}}\right) = (10^{-6}) \times \left(\frac{\text{Jy}}{\text{pixel}}\right) \times \left(\frac{1}{A_{\text{pixel}}}\right) \quad (15)$$

$$m\left(\frac{\text{Jy}}{\text{beam}}\right) = (2.665 \times 10^{-9}) \left(\frac{\text{Jy}}{\text{pixel}}\right) \times \left(\frac{\theta^2_{\text{HPBW}}}{A_{\text{pixel}}}\right), \quad (16)$$

where A_{pixel} (Sr) is the pixel area. All of the images were smoothed to match the resolution of $36\rlap{.}''4$, corresponding to the SPIRE 500 μm image. Equation (14) is fitted to the pixel-wise flux values of four images using "mpfit.pro" of the Markwardt IDL suite of functions (Markwardt 2009). Equal weight is given to the four input fluxes while fitting is performed.

ORCID iDs

Chakali Eswaraiah ⬤ https://orcid.org/0000-0003-4761-6139
Shih-Ping Lai ⬤ https://orcid.org/0000-0001-5522-486X
Wen-Ping Chen ⬤ https://orcid.org/0000-0003-0262-272X
M. Tamura ⬤ https://orcid.org/0000-0002-6510-0681
S. Sharma ⬤ https://orcid.org/0000-0001-5731-3057
Jia-Wei Wang ⬤ https://orcid.org/0000-0002-6668-974X
Jungmi Kwon ⬤ https://orcid.org/0000-0003-2815-7774
R. Purcell ⬤ https://orcid.org/0000-0002-7491-7386

References

Aannestad, P. A., & Purcell, E. M. 1973, ARA&A, 11, 309
Adams, F. C., Lada, C. J., & Shu, F. H. 1987, ApJ, 312, 788
Alves, F. O., Franco, G. A. P., & Girart, J. M. 2008, A&A, 486, L13
Anderson, L. D., Zavagno, A., Deharveng, L., et al. 2012, A&A, 542, A10
Andersson, B.-G., Lazarian, A., & Vaillancourt, J. E. 2015, ARA&A, 53, 501
André, P., Men'shchikov, A., Bontemps, S., et al. 2010, A&A, 518, L102
André, P., Minier, V., Gallais, P., et al. 2008, A&A, 490, L27
Andrews, S. M., & Williams, J. P. 2005, ApJ, 631, 1134
Arzoumanian, D., André, P., Didelon, P., et al. 2011, A&A, 529, L6
Arzoumanian, D., André, P., Peretto, N., & Könyves, V. 2013, A&A, 553, A119
Ballesteros-Paredes, J., Vázquez-Semadeni, E., & Scalo, J. 1999, ApJ, 515, 286
Bally, J., Yu, K. C., Rayner, J., & Zinnecker, H. 1998, AJ, 116, 1868
Barbosa, C. L., Damineli, A., Blum, R. D., & Conti, P. S. 2003, AJ, 126, 2411
Benedettini, M., Schisano, E., Pezzuto, S., et al. 2015, MNRAS, 453, 2036
Bessell, M. S., & Brett, J. M. 1988, PASP, 100, 1134
Beuther, H., Schilke, P., Sridharan, T. K., et al. 2002, A&A, 383, 892
Bisnovatyi-Kogan, G. S., & Silich, S. A. 1995, RvMP, 67, 661
Bodenheimer, P., Tenorio-Tagle, G., & Yorke, H. W. 1979, ApJ, 233, 85
Carpenter, J. M. 2001, AJ, 121, 2851
Caswell, J. L. 2004, MNRAS, 351, 279
Chandrasekhar, S., & Fermi, E. 1953, ApJ, 118, 113
Chapman, N. L., Goldsmith, P. F., Pineda, J. L., et al. 2011, ApJ, 741, 21
Chauhan, N., Ogura, K., Pandey, A. K., Samal, M. R., & Bhatt, B. C. 2011a, PASJ, 63, 795
Chauhan, N., Pandey, A. K., Ogura, K., et al. 2011b, MNRAS, 415, 1202
Churchwell, E., Povich, M. S., Allen, D., et al. 2006, ApJ, 649, 759
Churchwell, E., Watson, D. F., Povich, M. S., et al. 2007, ApJ, 670, 428
Cieza, L., Padgett, D. L., Stapelfeldt, K. R., et al. 2007, ApJ, 667, 308
Cohen, J. G., Persson, S. E., Elias, J. H., & Frogel, J. A. 1981, ApJ, 249, 481
Cox, N. L. J., Arzoumanian, D., André, P., et al. 2016, A&A, 590, A110
Danziger, I. J. 1974, ApJ, 193, 69
Davis, L., Jr., & Greenstein, J. L. 1951, ApJ, 114, 206
de Pree, C. G., Nysewander, M. C., & Goss, W. M. 1999, AJ, 117, 2902
Deharveng, L., Schuller, F., Anderson, L. D., et al. 2010, A&A, 523, A6
Deharveng, L., Zavagno, A., Samal, M. R., et al. 2015, A&A, 582, A1
Eswaraiah, C., Pandey, A. K., Maheswar, G., et al. 2011, MNRAS, 411, 1418
Eswaraiah, C., Pandey, A. K., Maheswar, G., et al. 2012, MNRAS, 419, 2587
Falceta-Gonçalves, D., & Monteiro, H. 2014, MNRAS, 438, 2853
Figuerêdo, E., Blum, R. D., Damineli, A., & Conti, P. S. 2002, AJ, 124, 2739
Franco, G. A. P., & Alves, F. O. 2015, ApJ, 807, 5
Frogel, J. A., & Persson, S. E. 1974, ApJ, 192, 351
Fukuda, N., & Hanawa, T. 2000, ApJ, 533, 911
Gaensler, B. M. 1998, ApJ, 493, 781
Griffin, M. J., Abergel, A., Abreu, A., et al. 2010, A&A, 518, L3
Gutermuth, R. A., Megeath, S. T., Myers, P. C., et al. 2009, ApJS, 184, 18
Hatano, H., Nishiyama, S., Kurita, M., et al. 2013, AJ, 145, 105
Heitsch, F., Zweibel, E. G., Mac Low, M.-M., Li, P., & Norman, M. L. 2001, ApJ, 561, 800
Hennebelle, P. 2003, A&A, 397, 381
Hennemann, M., Motte, F., Schneider, N., et al. 2012, A&A, 543, L3
Henney, W. J., Arthur, S. J., de Colle, F., & Mellema, G. 2009, MNRAS, 398, 157
Hill, T., Burton, M. G., Minier, V., et al. 2005, MNRAS, 363, 405
Hill, T., Motte, F., Didelon, P., et al. 2011, A&A, 533, A94
Hoq, S., Clemens, D. P., Guzmán, A. E., & Cashman, L. R. 2017, ApJ, 836, 199
Juvela, M., Ristorcelli, I., Pagani, L., et al. 2012, A&A, 541, A12
Kahn, F. D. 1958, RvMP, 30, 1058
Kandori, R., Kusakabe, N., Tamura, M., et al. 2006, Proc. SPIE, 6269
Kandori, R., Tamura, M., Kusakabe, N., et al. 2007, PASJ, 59, 487
Kauffmann, J., Bertoldi, F., Bourke, T. L., Evans, N. J., II, & Lee, C. W. 2008, A&A, 487, 993
Kusune, T., Sugitani, K., Miao, J., et al. 2015, ApJ, 798, 60
Kwon, J., Choi, M., Pak, S., et al. 2010, ApJ, 708, 758
Kwon, J., Tamura, M., Hough, J. H., et al. 2015, ApJS, 220, 17
Kwon, J., Tamura, M., Kandori, R., et al. 2011, ApJ, 741, 35
Lacy, J. H., Beck, S. C., & Geballe, T. R. 1982, ApJ, 255, 510
Landsman, W. B. 1993, in ASP Conf. Ser. 52, Astronomical Data Analysis Software and Systems II, ed. R. J. Hanisch, R. J. V. Brissenden, & J. Barnes (San Francisco, CA: ASP), 246
Lazarian, A., Andersson, B.-G., & Hoang, T. 2015, in Grain Alignment: Role of Radiative Torques and Paramagnetic Relaxation, ed. L. Kolokolova, J. Hough, & A.-C. Levasseur-Regourd (Cambridge: Cambridge Univ. Press), 81
Lee, H.-T., & Chen, W. P. 2007, ApJ, 657, 884

Li, H.-b., Fang, M., Henning, T., & Kainulainen, J. 2013, MNRAS, 436, 3707
Li, Z.-Y., & Nakamura, F. 2006, ApJL, 640, L187
Mackey, J. 2012, in ASP Conf. Ser. 459, Numerical Modeling of Space Plasma Slows (ASTRONUM 2011), ed. N. V. Pogorelov et al. (San Francisco, CA: ASP), 106
Mackey, J., & Lim, A. J. 2011a, MNRAS, 412, 2079
Mackey, J., & Lim, A. J. 2011b, BSRSL, 80, 391
Mackey, J., & Lim, A. J. 2013, HEDP, 9, 1
Maercker, M., Burton, M. G., & Wright, C. M. 2006, A&A, 450, 253
Mampaso, A., Vilchez, J. M., Pismis, P., & Phillips, J. P. 1987, RMxAA, 14, 474
Markwardt, C. B. 2009, in ASP Conf. Ser. 411, Astronomical Data Analysis Software and Systems XVIII, ed. D. A. Bohlender, D. Durand, & P. Dowler (San Francisco, CA: ASP), 251
Martin, P. G. 1974, ApJ, 187, 461
Medhi, B. J., Maheswar, G., Pandey, J. C., Kumar, T. S., & Sagar, R. 2008, MNRAS, 388, 105
Medhi, B. J., Maheswar, G., Pandey, J. C., Tamura, M., & Sagar, R. 2010, MNRAS, 403, 1577
Medhi, B. J., & Tamura, M. 2013, MNRAS, 430, 1334
Meyer, M. R., Calvet, N., & Hillenbrand, L. A. 1997, AJ, 114, 288
Mezger, P. G., Sievers, A. W., Haslam, C. G. T., et al. 1992, A&A, 256, 631
Minier, V., Tremblin, P., Hill, T., et al. 2013, A&A, 550, A50
Moneti, A., Pipher, J. L., Helfer, H. L., McMillan, R. S., & Perry, M. L. 1984, ApJ, 282, 508
Motoyama, K., Umemoto, T., Shang, H., & Hasegawa, T. 2013, ApJ, 766, 50
Mouschovias, T. C. 1978, in IAU Colloq. 52: Protostars and Planets, ed. T. Gehrels (Cambridge: Cambridge Univ. Press), 209
Nagashima, C., Nagayama, T., Nakajima, Y., et al. 1999, in Star Formation 1999, ed. T. Nakamoto (Nobeyama: Nobeyama Radio Observatory), 397
Nagayama, T., Nagashima, C., Nakajima, Y., et al. 2003, Proc. SPIE, 4841, 459
Nakamura, F., & Li, Z.-Y. 2007, ApJ, 662, 395
Nakamura, F., & Li, Z.-Y. 2008, ApJ, 687, 354
Nakamura, F., & Li, Z.-Y. 2011, ApJ, 740, 36
Nutter, D., Kirk, J. M., Stamatellos, D., & Ward-Thompson, D. 2008, MNRAS, 384, 755
Ostriker, E. C., Stone, J. M., & Gammie, C. F. 2001, ApJ, 546, 980
Palmeirim, P., André, P., Kirk, J., et al. 2013, A&A, 550, A38
Pandey, A. K., Eswaraiah, C., Sharma, S., et al. 2013, ApJ, 764, 172
Pandey, A. K., Sharma, S., Ogura, K., et al. 2008, MNRAS, 383, 1241
Pavel, M. D., & Clemens, D. P. 2012, ApJ, 760, 150
Peretto, N., André, P., Könyves, V., et al. 2012, A&A, 541, A63
Pereyra, A., & Magalhães, A. M. 2004, ApJ, 603, 584
Pereyra, A., & Magalhães, A. M. 2007, ApJ, 662, 1014
Persi, P., Roth, M., Tapia, M., Ferrari-Toniolo, M., & Marenzi, A. R. 1994, A&A, 282, 474
Planck Collaboration, Adam, R., Ade, P. A. R., et al. 2016a, A&A, 586, A135
Planck Collaboration, Ade, P. A. R., Aghanim, N., et al. 2016b, A&A, 586, A136
Planck Collaboration, Aghanim, N., Alves, M. I. R., et al. 2016c, A&A, 586, A137
Poglitsch, A., Waelkens, C., Geis, N., et al. 2010, A&A, 518, L2
Purcell, C. R., Minier, V., Longmore, S. N., et al. 2009, A&A, 504, 139
Roccatagliata, V., Preibisch, T., Ratzka, T., & Gaczkowski, B. 2013, A&A, 554, A6
Santos, F. P., Franco, G. A. P., Roman-Lopes, A., Reis, W., & Román-Zúñiga, C. G. 2014, ApJ, 783, 1
Santos, F. P., Roman-Lopes, A., & Franco, G. A. P. 2012, ApJ, 751, 138
Schleuning, D. A. 1998, ApJ, 493, 811
Serkowski, K., Mathewson, D. S., & Ford, V. L. 1975, ApJ, 196, 261
Serón Navarrete, J. C., Roman-Lopes, A., Santos, F. P., Franco, G. A. P., & Reis, W. 2016, MNRAS, 462, 2266
Simpson, R. J., Povich, M. S., Kendrew, S., et al. 2012, MNRAS, 424, 2442
Skrutskie, M. F., Cutri, R. M., Stiening, R., et al. 2006, AJ, 131, 1163
Smith, N., Povich, M. S., Whitney, B. A., et al. 2010, MNRAS, 406, 952
Smith, R. J., Glover, S. C. O., & Klessen, R. S. 2014, MNRAS, 445, 2900
Staude, H. J., & Elsässer, H. 1993, A&Ar, 5, 165
Strafella, F., Elia, D., Campeggio, L., et al. 2010, ApJ, 719, 9
Sugitani, K., Fukui, Y., & Ogura, K. 1991, ApJS, 77, 59
Sugitani, K., Nakamura, F., Tamura, M., et al. 2010, ApJ, 716, 299
Sugitani, K., Nakamura, F., Watanabe, M., et al. 2011, ApJ, 734, 63
Sugitani, K., & Ogura, K. 1994, ApJS, 92, 163
Tilley, D. A., & Pudritz, R. E. 2003, ApJ, 593, 426
Tomisaka, K. 1992, PASJ, 44, 177
Torii, K., Hasegawa, K., Hattori, Y., et al. 2015, ApJ, 806, 7
Townsley, L. K. 2009, in An X-ray Tour of Massive-star-forming Regions with Chandra, ed. M. Livio & E. Villaver (Cambridge: Cambridge Univ. Press), 60
Townsley, L. K., Broos, P. S., Chu, Y.-H., et al. 2011, ApJS, 194, 16
Townsley, L. K., Broos, P. S., Garmire, G. P., et al. 2014, ApJS, 213, 1
Vaillancourt, J. E., Dowell, C. D., Hildebrand, R. H., et al. 2008, ApJL, 679, L25
van Marle, A. J., Meliani, Z., & Marcowith, A. 2015, A&A, 584, A49
Wardle, J. F. C., & Kronberg, P. P. 1974, ApJ, 194, 249
Ward-Thompson, D., Pattle, K., Bastien, P., et al. 2017, arXiv:1704.08552
White, G. J., & Fridlund, C. V. M. 1992, A&A, 266, 452
Williams, R. J. R., Ward-Thompson, D., & Whitworth, A. P. 2001, MNRAS, 327, 788
Wisniewski, J. P., Bjorkman, K. S., Magalhães, A. M., & Pereyra, A. 2007, ApJ, 664, 296
Zhang, C.-P., Li, G.-X., Wyrowski, F., et al. 2016, A&A, 585, A117
Zinnecker, H., & Yorke, H. W. 2007, ARA&A, 45, 481